Monthly Notices of the ROYAL ASTRONOMICAL SOCIETY
MNRAS **444,** 3388–3407 (2014) doi:10.1093/mnras/stt2496

The ATLAS^{3D} project – XXVI. H I discs in real and simulated fast and slow rotators

Paolo Serra,[1,2]★ Ludwig Oser,[3,4] Davor Krajnović,[5] Thorsten Naab,[3] Tom Oosterloo,[1,6] Raffaella Morganti,[1,6] Michele Cappellari,[7] Eric Emsellem,[8,9] Lisa M. Young,[10] Leo Blitz,[11] Timothy A. Davis,[8] Pierre-Alain Duc,[12] Michaela Hirschmann,[13] Anne-Marie Weijmans,[14,15]† Katherine Alatalo,[11,16] Estelle Bayet,[7] Maxime Bois,[8,9] Frédéric Bournaud,[12] Martin Bureau,[7] Alison F. Crocker,[17] Roger L. Davies,[7] P. T. de Zeeuw,[8,18] Sadegh Khochfar,[19,20] Harald Kuntschner,[8] Pierre-Yves Lablanche,[8,9] Richard M. McDermid,[21] Marc Sarzi[22] and Nicholas Scott[23,24]

Affiliations are listed at the end of the paper

Accepted 2013 December 20. Received 2013 November 28; in original form 2013 October 20

ABSTRACT

One quarter of all nearby early-type galaxies (ETGs) outside Virgo host a disc/ring of H I with size from a few to tens of kpc and mass up to $\sim 10^9$ M$_\odot$. Here we investigate whether this H I is related to the presence of a stellar disc within the host making use of the classification of ETGs in fast and slow rotators (FR/SR). We find a large diversity of H I masses and morphologies within both families. Surprisingly, SRs are detected as often, host as much H I and have a similar rate of H I discs/rings as FRs. Accretion of H I is therefore not always linked to the growth of an inner stellar disc. The weak relation between H I and stellar disc is confirmed by their frequent kinematical misalignment in FRs, including cases of polar and counterrotating gas. In SRs the H I is usually polar. This complex picture highlights a diversity of ETG formation histories which may be lost in the relative simplicity of their inner structure and emerges when studying their outer regions. We find that Λ CDM hydrodynamical simulations have difficulties reproducing the H I properties of ETGs. The gas discs formed in simulations are either too massive or too small depending on the star formation feedback implementation. Kinematical misalignments match the observations only qualitatively. The main point of conflict is that nearly all simulated FRs and a large fraction of all simulated SRs host corotating H I. This establishes the H I properties of ETGs as a novel challenge to simulations.

Key words: ISM: kinematics and dynamics – galaxies: elliptical and lenticular, cD – galaxies: evolution – galaxies: formation – galaxies: kinematics and dynamics.

1 INTRODUCTION

The observation of both neutral hydrogen (H I) and molecular gas (H_2, traced by CO) has shown that early-type galaxies (E/S0s, hereafter ETGs), while on average gas poorer than spirals, can in some cases host a significant mass of cold gas (for early H I studies see, e.g. Gallagher, Faber & Balick 1975; Bieging & Biermann 1977; Knapp et al. 1977; Knapp, Turner & Cunniffe 1985; Wardle & Knapp 1986; for CO see Wiklind & Henkel 1989; Lees et al. 1991). What has remained unclear until recently is whether gas-rich ETGs are peculiar, rare objects or represent a significant fraction of the overall population (e.g. van Gorkom & Schiminovich 1997). This question has now been answered by large H I and H_2 surveys of morphologically selected ETGs carried out as part of the ATLAS^{3D} project (Cappellari et al. 2011a, hereafter Paper I).

In Serra et al. (2012, hereafter Paper XIII) we show that ∼40 per cent of all ETGs outside the Virgo cluster and ∼10 per cent inside Virgo host H I down to a mass of $\sim 10^7$ M$_\odot$ and a column

★ E-mail: paolo.serra@csiro.au
† Dunlap Fellow.

density of $\sim 3 \times 10^{19}$ cm^{-2}, placing recent, previous results (Morganti et al. 2006; di Serego Alighieri et al. 2007; Grossi et al. 2009; Oosterloo et al. 2010) on a strong statistical basis. We find that in $\sim 2/3$ of all detections (and 1/4 of all ETGs outside Virgo) the H I is distributed in a low-column-density disc or ring with size from a few to tens of kpc, and mass from $\sim 10^7$ to more than 10^9 M$_\odot$ (see also van Driel & van Woerden 1991; Oosterloo et al. 2007). The remaining detected ETGs host H I on an unsettled configuration which usually reveals recent dynamical interaction within a group.

Concerning molecular gas, Young et al. (2011, hereafter Paper IV) detect CO in 22 per cent of all ETGs independent of galaxy luminosity or environment, with $M(H_2)$ between $\sim 10^7$ M$_\odot$ (the typical sensitivity of their data) and $\sim 10^9$ M$_\odot$ (for recent, previous surveys of smaller samples see Combes, Young & Bureau 2007; Sage, Welch & Young 2007). Follow-up interferometric observations show that this gas is mostly distributed on discs and rings with typical radius ~ 1 kpc, just a fraction of the galaxy effective radius (Alatalo et al. 2013; Davis et al. 2013).

Taken together, these studies establish that about half of all ETGs host between $\sim 10^7$ and $\sim 10^9$ M$_\odot$ of cold gas (atomic and/or molecular) usually settled within the galaxy potential. Very sensitive observations are required to reach such a detection rate (for example, this is significantly higher than in the recent surveys of massive galaxies by Catinella et al. 2010 and Saintonge et al. 2011) but when these are performed we find that ETGs with a significant mass of cold gas are not peculiar, rare systems. The obvious implication is that in order to understand the assembly of ETGs as a family we need to understand how they get or retain their gas and what impact this has on the host, on its star formation history and on its structure. Here we focus on the latter aspect.

In most previous studies of this kind ETGs are simply divided into ellipticals and lenticulars. When this is done, molecular gas is almost exclusively found in lenticulars (Lees et al. 1991; Welch, Sage & Young 2010, Paper IV), consistent with the fact that CO is invariably associated with dust lanes. Furthermore, H I seems to be more abundant in lenticular than in elliptical objects at a typical M(H I) sensitivity of $\sim 10^9$ M$_\odot$ (Roberts 1975; Wardle & Knapp 1986; Bregman, Hogg & Roberts 1992; Sadler 2001) although more sensitive observations of smaller samples do not reveal any significant difference (Grossi et al. 2009; Oosterloo et al. 2010). One complication is that the distinction between ellipticals and lenticulars can be ambiguous and is affected by projection effects (Jorgensen & Franx 1994). A more robust and physically meaningful approach is to classify ETGs on the basis of their internal kinematics (e.g. Davies et al. 1983; Cappellari et al. 2007; Emsellem et al. 2007).

In this context a key result of the ATLAS^{3D} project is that the vast majority of all ETGs ($\sim$85 per cent) are structurally similar to spirals. They rotate like discs (Krajnović et al. 2011, hereafter Paper II), can be described as a family of oblate rotators on the $\lambda_R - \epsilon$ diagram (Emsellem et al. 2011, hereafter Paper IIII) and cover the same range of intrinsic flattening and bulge-to-disc ratio of Sa to Sc spirals (Cappellari et al. 2011b, 2013b, hereafter Paper VII and Paper XX, respectively; Krajnović et al. 2013a; Weijmans et al. 2013; see also Laurikainen et al. 2011; Kormendy & Bender 2012). We call these ETGs fast rotators (FRs). In practice, FRs include nearly all classical lenticulars plus a large number of galaxies morphologically misclassified as ellipticals because of unfavourable viewing angle (Paper III). The evolutionary history of most FRs must include the growth and survival of a stellar disc following accretion of cold gas from the surrounding medium as well as gas-rich minor and major mergers (Khochfar et al. 2011, hereafter Paper VIII; Naab et al. 2014, hereafter Paper XXV).

The remaining $\sim$15 per cent of all ETGs do not exhibit the disc-like stellar rotation observed in FRs and occupy a region of the $\lambda_R - \epsilon$ diagram corresponding to intrinsically lower specific angular momentum and flattening (Paper III). We call these galaxies slow rotators (SRs). We find that SRs form a heterogeneous family including systems with no rotation at all, non-disc-like rotation and kinematically distinct cores (KDCs). Massive SRs are thought to grow via (a small number of) major mergers at $z > 1$, which lower the system angular momentum and may create a KDC, followed by many minor mergers with low gas fraction, which preserve the KDC and make the stellar body rounder (Naab, Johansson & Ostriker 2009; Bois et al. 2011, hereafter Paper VI; Paper VIII, Paper XXV). This sequence of events is most likely to occur in a dense environment, in agreement with the increased fraction of SRs in the centre of the Virgo cluster (Paper VII).

Within this picture one may naively think that SRs should lack a significant cold-gas phase, unlike FRs. Indeed, Paper IV shows that the CO detection rate is much lower in SRs than in FRs. However, the situation is not necessarily so simple. For example, the detection of kinematically misaligned ionized-gas (Davis et al. 2011, hereafter Paper X), cold dust (Smith et al. 2012) and stellar nuclear cusps (Krajnović et al. 2013b, hereafter Paper XXIII) in SRs suggests that they too can accrete some gas during their life; and simulations show that at least some SRs may have formed in gas-rich mergers (Paper VI, Paper XXV). Furthermore, the mere fact that FRs are found at basically all environment densities (Paper VII) implies that there must be a large variety of evolutionary histories leading to their formation, and therefore potentially a large variety of resulting cold-gas properties.

All that is required to mark the visual difference between a FR and a spiral at $z = 0$ is that the former should have lower star formation rate surface density on the stellar disc. In other words, they should be quenched owing to a lower $M_{\rm gas}/M_\star$ and/or star formation efficiency within the stellar body. Observations indicate that such quenching may be related to the growth of the stellar bulge: the cold gas content of the stellar body decreases as the bulge becomes more dominant (Catinella et al. 2010; Saintonge et al. 2011, Paper XX) and, additionally, the bulge may stabilize the remaining gas against star formation (Kawata, Cen & Ho 2007; Martig et al. 2009; Saintonge et al. 2012; Martig et al. 2013). Yet it is still possible for a FR to host a large mass of cold gas well outside the stellar body and at low surface density (e.g. Morganti et al. 2006; Oosterloo et al. 2007, Paper XIII). Such gas distributions are indicative that there are many ways of making a FR and that this information, lost in the apparent homogeneity of their shape and stellar kinematics, may emerge when observing their cold-gas phase. Furthermore, these tenuous gas systems are only weakly bound to the host and hence are easily perturbed. Their actual morphology is therefore a sensitive probe of the past dynamical history of the host, and indeed in Paper XIII we show that the H I morphology varies systematically with the density of the environment.

In this spirit we study here the H I properties of ETGs as a function of their structure within the context of the ATLAS^{3D} project. The few previous attempts in this direction reveal no clear relation between H I and ETG structure but are based on significantly smaller samples (Morganti et al. 2006; Oosterloo et al. 2010). Here we aim at clarifying the situation by studying the large ATLAS^{3D} H I sample. We describe the sample and the H I data in Section 2, discuss H I detection rate, mass and morphology as a function of galaxy structure in Section 3, analyse the kinematical misalignment

between H I and stars in Section 4, perform for the first time a comparison to the predictions of ΛCDM hydrodynamical simulations in Section 5 and summarize the results in Section 6.

2 SAMPLE AND H I SURVEY

The ATLAS^{3D} H I sample and the radio observations which this study is based on are described in detail in Paper XIII. Here we provide a short summary. We study a subset of the full ATLAS^{3D} sample of ETGs (Paper I; distance < 42 Mpc, $M_K < -21.5$). This subset includes all galaxies with declination $\delta \geq 10^\circ$ except the four objects closest to Virgo A, resulting in a volume-limited sample of 166 ETGs (127 outside the Virgo cluster). We obtain Westerbork Synthesis Radio Telescope H I data for most of them either as part of the ATLAS^{3D} project or from previous projects (Morganti et al. 2006; Józsa et al. 2009; Oosterloo et al. 2010). We make use of Very Large Array data for 1 galaxy with H I (Chung et al. 2009) and of Arecibo spectra for 20 galaxies (all undetected; Giovanelli et al. 2005).

As mentioned in Section 1, our Westerbork observations allow us to detect H I down to a column density of a few times 10^{19} cm^{-2} and a mass of $\sim 10^7$ M$_\odot$. We detect H I associated with the target ETG in 53 galaxies (49 outside Virgo). In Paper XIII we classify detected ETGs in the following classes on the basis of the H I morphology: D = large discs (14 objects); R = large rings[1] (10); d = small discs (10); u = unsettled distributions (14); c = gas clouds (5). Gas distributions characterized by ordered rotation (D, R and d classes) are therefore the most common ones among H I-rich ETGs, amounting to 2/3 of all detections and 1/4 of all ETGs outside Virgo. As discussed in Paper XIII, the above H I classes are a way to simplify the observed continuum of gas morphologies, with a number of objects being intermediate (or in transition) between classes. We make use of the H I classes D, R, d, u and c in the rest of this paper.

In Paper XIII we show H I images of all detections. Each image is obtained after creating a mask including all emission in the corresponding H I cube. The images shown in Paper XIII are the zeroth moment of the masked cubes. In this paper we show and analyse for the first time the H I velocity fields obtained as the first moment of the same masked cubes.

3 RELATION BETWEEN H I AND ETG INNER STRUCTURE

In this section we investigate whether the H I detection rate, mass and morphology of ETGs are related to their stellar kinematics as well as position on the $\lambda_R - \epsilon$ diagram[2] and mass–size plane. In particular, we make use of the kinematical classification presented in Paper II. In that paper ETGs are divided in the following classes based on a quantitative analysis of their stellar velocity field:[3] $a_\star$ = no rotation; $b_\star$ = some rotation but with a velocity field not consistent with that of a rotating disc; $c_\star$ = KDC; $d_\star$ = two counterrotating stellar discs; $e_\star$ = velocity field consistent with that of a rotating disc. These classes are important to understand the classification of ETGs into FRs and SRs discussed in Section 1. In Paper III we define FRs and SRs as galaxies above and below the line $\lambda_R = 0.31\sqrt{\epsilon}$ on the $\lambda_R - \epsilon$ diagram, respectively. FRs and $e_\star$ ETGs are essentially the same family and represent ∼85 per cent of all objects. On the other hand, the SR family is very heterogeneous and includes galaxies in all other groups ($a_\star$ to $d_\star$).

3.1 Fast versus slow rotators

Fig. 1 shows all galaxies on the $\lambda_R - \epsilon$ diagram. In this figure we indicate galaxies with different stellar kinematics and H I morphology using different colours and markers, respectively. To first order Fig. 1 confirms the results of Morganti et al. (2006) and Oosterloo et al. (2010): the relation between H I properties and galaxy structure is not a simple one.

We detect H I in galaxies at all locations on the $\lambda_R - \epsilon$ diagram where there are ETGs, both FRs and SRs. Many of the H I discs and rings (D, R and d) are hosted by flat, nearly edge-on FRs (top right of the diagram) and their lower-inclination counterparts (at lower values of λ_R and ϵ). This is reasonable as these galaxies have a pronounced stellar disc component and therefore must have experienced a considerable level of dissipation during their assembly. Their current H I discs/rings may be a remnant of that process. The more detailed analysis of Section 4 shows that this is indeed the case for about half of all gas-rich FRs, but also that in the remaining half the gas accretion episode traced by H I does not seem to be related to the formation of the current stellar disc.

What might be more surprising is to find H I also among SRs ($a_\star$, $b_\star$ and $c_\star$ objects only) and that in some of them the detected H I is distributed on a large disc or ring. This indicates that SRs too can experience gas accretion and dissipative processes during their formation, and gas-poor evolutionary paths are not the only way to make a galaxy with this internal structure. A similar conclusion is reached by Paper X based on the misalignment between ionized-gas and stellar kinematics in these galaxies within $\sim 1\,R_e$, by Smith et al. (2012) based on the frequent detection of cold dust in SRs, by Paper XXIII based on the existence of SRs with a cuspy nuclear light profile, and by both idealized and ΛCDM hydrodynamical simulations (Paper VI, Paper XXV). Additional observations such as very deep optical imaging may provide further clues about the formation of SRs in presence of a cold gas component (Duc et al. 2011).

These qualitative results are illustrated in more quantitative terms in Table 1 for the full sample and in Table 2 for non-Virgo galaxies only. Within the limited statistics available for SRs (and for classes $a_\star$ to $d_\star$), their H I detection rate is the same as that of FRs (and $e_\star$ objects). Namely, we detect H I in 41 ± 14 per cent of all SRs and 31 ± 5 per cent of all FRs, while outside Virgo the detection rate becomes 50 ± 18 per cent for SRs and 37 ± 6 per cent for FRs (error bars assume a binomial distribution). The fraction of galaxies hosting a rotating H I distribution (H I classes D, R and d) is 18 ± 9 per cent for SRs and 21 ± 4 per cent for FRs over the full sample, while outside Virgo it becomes 25 ± 13 per cent for SRs and 25 ± 5 per cent for FRs.

The above paragraph describes the H I properties (detection rate and morphology) as a function of stellar kinematics. A complementary approach is to examine the stellar kinematics as a function of H I properties, but also in this case Tables 1 and 2 show that there is no clear trend. Within each H I class (including that formed by all undetected ETGs) the fraction of SRs and FRs is consistent with the global values of ∼15 and ∼85 per cent, respectively. The same is true considering all galaxies with a settled H I distribution

[1] In fact, in Paper XIII we group Ds and Rs in a single class. In table 1 of that paper we indicate galaxies where the H I is distributed on a ring. Here we use that table as a basis for the division into D and R objects.

[2] We adopt the λ_R and ϵ measurements obtained within a 1 R_e aperture in Paper III. Note that not all galaxies have their stellar kinematics measured out to 1 R_e, as discussed in that paper.

[3] Note the addition of a ⋆ subscript to the kinematical classes name to avoid confusion with the H I classes defined in Section 2.

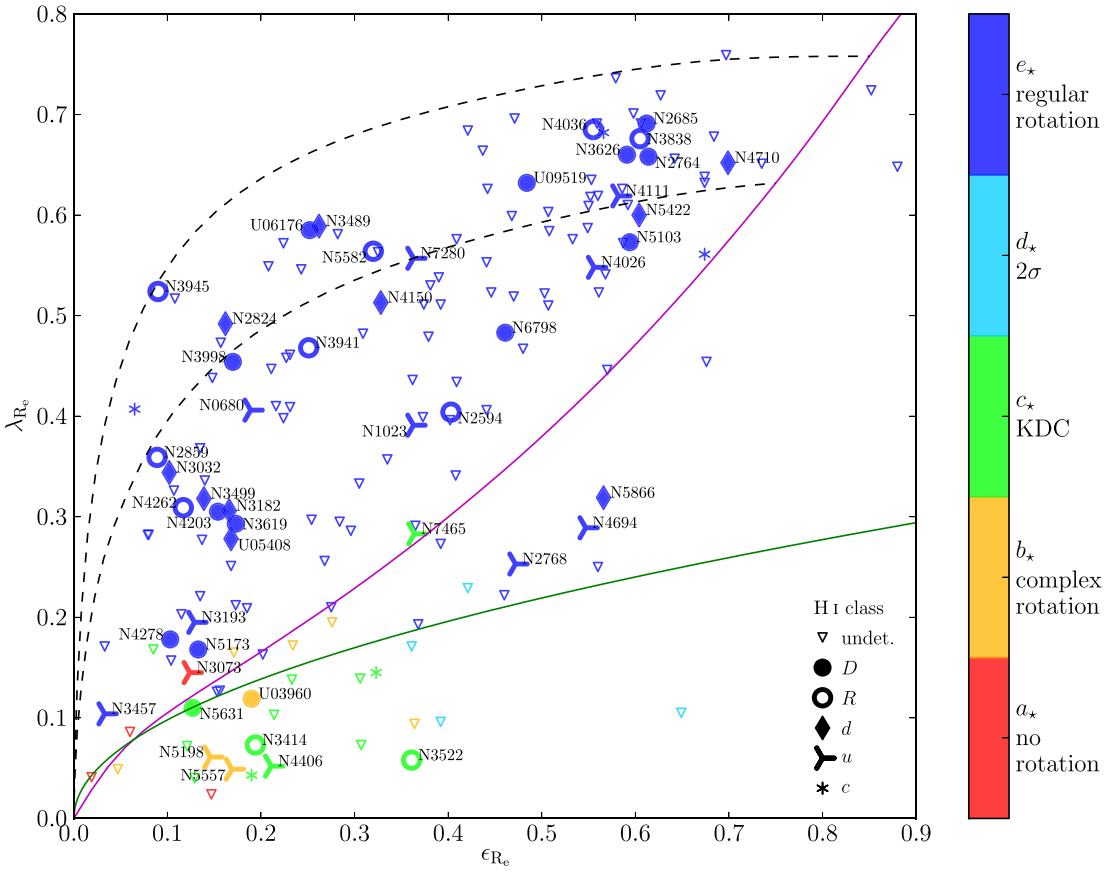

Figure 1. H I on the $\lambda_R - \epsilon$ diagram. The colour scheme represents the kinematical classification of ETGs presented in Paper II. The markers shape represent the H I morphology as in Paper XIII with the small modification described in Section 2. The magenta line represents the edge-on view of anisotropic, oblate models with $\beta = 0.65 \times \epsilon$ (Cappellari et al. 2007), and the black dashed lines represent the models with $\epsilon = 0.75$ and 0.85 viewed under all possible inclinations from edge-on (top right) to face-on (bottom left). The green line represents the empirical separation between FRs and SRs $\lambda_R = 0.31\sqrt{\epsilon}$ proposed in Paper III. We indicate the name of all H I detections except that of *c* galaxies.

Table 1. Number of galaxies in the various H I morphological classes (Paper XIII) as a function of stellar kinematics class (Paper III) and SR/FR classification (Paper II) for the full ATLAS^{3D} H I sample.

Full Sample		All	$a_\star$	$b_\star$	$c_\star$	$d_\star$	$e_\star$	SR	FR
	All	166	4	8	14	4	136	22	144
	Undet.	113	3	5	7	4	94	13	100
	Det.	53	1	3	7	0	42	9	44
H I	*D*	14	0	1	1	0	12	2	12
	R	10	0	0	2	0	8	2	8
	d	10	0	0	0	0	10	0	10
	u	14	1	2	2	0	9	3	11
	c	5	0	0	2	0	3	2	3

Table 2. Number of galaxies in the various H I morphological classes (Paper XIII) as a function of stellar kinematics class (Paper III) and SR/FR classification (Paper II) for non-Virgo ETGs in the ATLAS^{3D} H I sample.

Outside Virgo		All	$a_\star$	$b_\star$	$c_\star$	$d_\star$	$e_\star$	SR	FR
	All	127	2	7	11	1	106	16	111
	Undet.	78	1	4	5	1	67	8	70
	Det.	49	1	3	6	0	39	8	41
H I	*D*	14	0	1	1	0	12	2	12
	R	9	0	0	2	0	7	2	7
	d	9	0	0	0	0	9	0	9
	u	12	1	2	1	0	8	2	10
	c	5	0	0	2	0	3	2	3

together (*D*, *R* and *d*). We also compare the $\lambda_R/(0.31\sqrt{\epsilon})$ distribution of $D + R + d$ ETGs to that of undetected + *c* objects[4] and find that they are indistinguishable – according to a two-sample KS test the probability that the two samples are not drawn from the same parent distribution is 78 per cent, insufficient to claim a significant difference.

The only possible exception to this lack of trends is that small H I discs (*d*) include no SRs. This is consistent with the fact that H I in these galaxies seems to be strongly linked to the presence of molecular gas and star formation within a stellar disc (Paper XIII). However, the number of *d*s is low and only ∼1 SR would be expected among them based on the global SR fraction. Better statistics would therefore be needed to confirm this result.

[4] In this context *c* ETGs can be grouped together with non-detections since M(H I) is very low and the detected gas does not appear obviously associated with the host (Paper XIII).

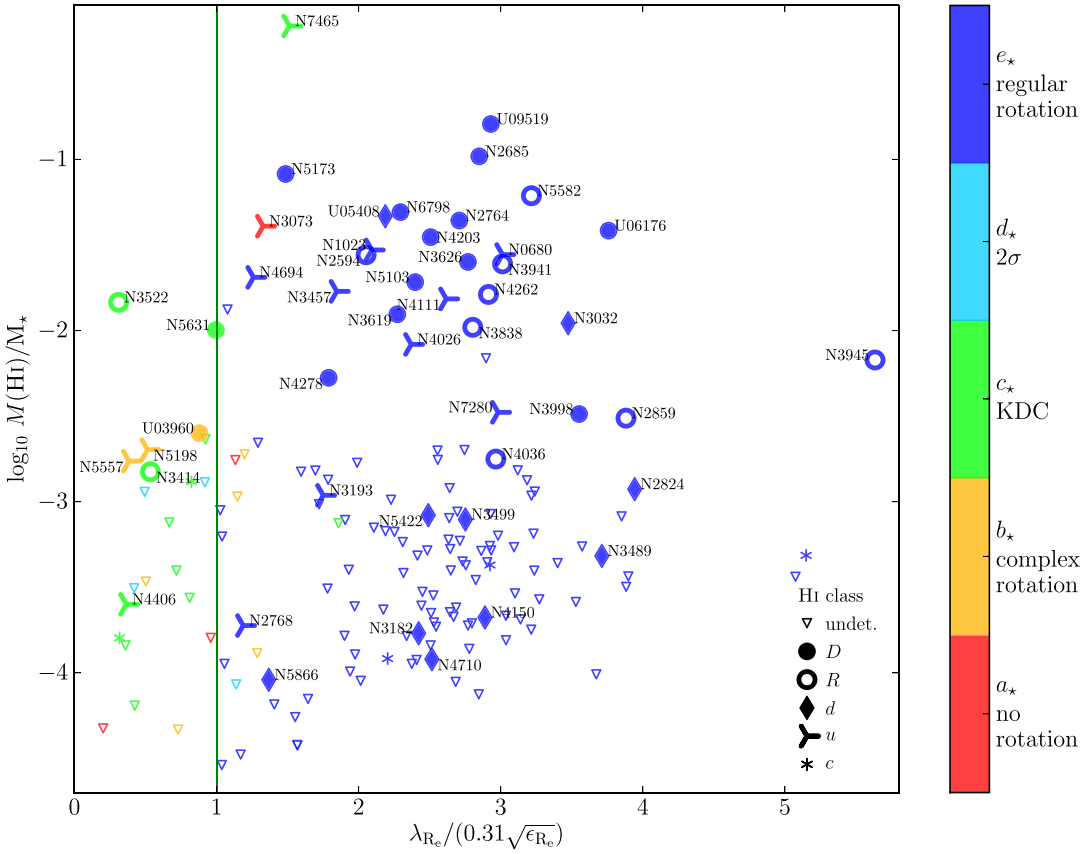

Figure 2. $M(\mathrm{H\,I})/M_\star$ plotted against the ratio $\lambda_R/(0.31\sqrt{\epsilon})$, such that SRs and FRs are found to the left and right of the green, vertical line, respectively. Colours and markers are as in Fig. 1.

Another important quantity to analyse is the H I mass. Fig. 2 shows the $M(\mathrm{H\,I})/M_\star$ ratio plotted against the $\lambda_R/(0.31\sqrt{\epsilon})$ ratio. Here and in the rest of this paper we adopt for $M_\star$ the value derived by Cappellari et al. (2013a, hereafter Paper XV) based on dynamical modelling – M_{JAM} in that paper.[5] One galaxy, PGC 071531, has no reliable $M_\star$ measurement and is excluded from this analysis. Fig. 2 shows that H I-detected SRs are found over a wide range of $M(\mathrm{H\,I})/M_\star$. They seem not to reach the large $M(\mathrm{H\,I})/M_\star$ values allowed for FRs but the overall low number of SRs makes this difference statistically insignificant. For example, the fraction of galaxies with $M(\mathrm{H\,I})/M_\star \geq 0.002$ is 23 ± 10 per cent within the SR family and 24 ± 4 per cent for FRs. These fractions remain comparable to one another if we consider ETGs outside Virgo only, and these (and the following) results do not change if we adopt a different $M(\mathrm{H\,I})/M_\star$ threshold. Conversely, we define two ETG subsamples with $M(\mathrm{H\,I})/M_\star$ above and below 0.002, including 39 and 126 galaxies, respectively. We find that they contain a similar fraction of SRs consistent with the global value of ∼15 per cent, both considering all galaxies or non-Virgo galaxies only. Finally, according to a two-sample KS test the probability that the $\lambda_R/(0.31\sqrt{\epsilon})$ distributions of the two subsamples are not drawn from the same parent distribution is just 4 per cent.

[5] The results discussed in this section do not change if we normalize $M(\mathrm{H\,I})$ to L_K. This follows from the fact that the distribution of $M_\star/L_K$ ratio is very narrow for ETGs, peaking at 1.2 $M_\odot/L_\odot$ and with an rms of 0.4 $M_\odot/L_\odot$. This scatter is insufficient to significantly alter a plot like the one showed in Fig. 2, where galaxies spread over ∼3 orders of magnitude in $M(\mathrm{H\,I})/M_\star$.

3.2 H I properties within the FR family

Considering now FRs alone, we find no systematic variation of H I properties as a function of position on the $\lambda_R - \epsilon$ diagram. Specifically, we compare intrinsically flatter FRs to rounder ones. We do this by considering $e_\star$ galaxies only and splitting them in two groups above and below the line of 0.75 intrinsic ellipticity, respectively (see Fig. 1; we comment below on alternative ways of defining flat and round galaxies). This results in 47 'flat' and 89 'round' $e_\star$ ETGs (39 and 67 outside Virgo, respectively). We detect H I in 32 ± 8 per cent of all flat objects and 30 ± 6 per cent of all round ones. The detection rate of rotating H I distributions (*D*, *R* and *d* objects) is 26 ± 7 and 20 ± 5 per cent, respectively, with both flat and round ETGs exhibiting a mix of *D*, *R* and *d* objects. No significant difference emerges if we consider non-Virgo galaxies only.

Conversely, the fraction of flat and round $e_\star$ ETGs does not vary significantly as a function of H I class (also when grouping together all *D*, *R* and *d* systems). Within the error bars, we always find ∼35 per cent of flat objects and ∼65 per cent of round galaxies. Furthermore, the $\lambda_R/\lambda_{R,\,\epsilon=0.75}$ distribution of galaxies with an H I disc or ring (*D*, *R* and *d*) is statistically undistinguishable from that of galaxies with no H I (undetected and *c*). The two-sample KS-test probability that the two distributions are not drawn from the same parent distribution is 38 per cent.

We also investigate possible variations of $M(\mathrm{H\,I})/M_\star$ within the FR family. We find that 19 ± 6 per cent of all flat galaxies have $M(\mathrm{H\,I})/M_\star \geq 0.002$, comparable to the 26 ± 5 per cent found for round objects. Conversely, we define an H I-rich and an H I-poor subsample of $e_\star$ ETGs adopting the same $M(\mathrm{H\,I})/M_\star$ separation as

above. The two samples include 32 and 103 galaxies, respectively. The fraction of flat objects in the two groups is comparable (28 ± 9 and 37 ± 6 per cent, respectively). Finally, a two-sample KS test gives a probability of just 10 per cent that the $\lambda_R/\lambda_{R,\,\epsilon\,=\,0.75}$ distributions of the two subsamples are not drawn from the same parent distribution.

The definition of flat and round FRs adopted above relies on a simple de-projection of galaxies' shape along model lines on the $\lambda_R - \epsilon$ diagram. A more accurate estimate of the intrinsic ellipticity of ETGs is derived in Paper XX based on the modelling presented in Paper XV and on the ellipticity measurement at large radius reported in Paper II. However, we have verified that using these intrinsic ellipticity values does not change any of the above conclusions. Flat and round FRs keep having equal H I detection rates as well as equal fractions of H I discs and of galaxies with $M(\mathrm{H\,I})/M_\star \geq 0.002$. Similarly, the distribution of FR intrinsic ellipticity does not change as a function of H I mass or morphology.

3.3 Mass–size plane

Although the $\lambda_R - \epsilon$ diagram is very useful to separate SRs from FRs, Paper XX shows that a number of key ETG properties vary in a much clearer way on the mass–size plane instead. In particular, properties linked to the star formation history of galaxies such as their mass-to-light ratio, optical colour, Hβ absorption and $M(\mathrm{H_2})/M_\star$ ratio correlate with bulge-to-disc ratio (traced by velocity dispersion) on this plane. We therefore investigate whether the ETG H I properties too exhibit any systematic variation on the mass–size plane.

Fig. 3 shows all galaxies on the mass–size plane of Paper XX. This figure does not show any clear trend other than the decrease of the typical $M(\mathrm{H\,I})$ value and the prevalence of disturbed H I morphologies at high galaxy mass, already reported in Paper XIII. As with Fig. 2, the main observational result is a very large scatter of H I properties, reinforcing our conclusion that H I does not appear to be linked in any clear way to the inner galaxy structure.

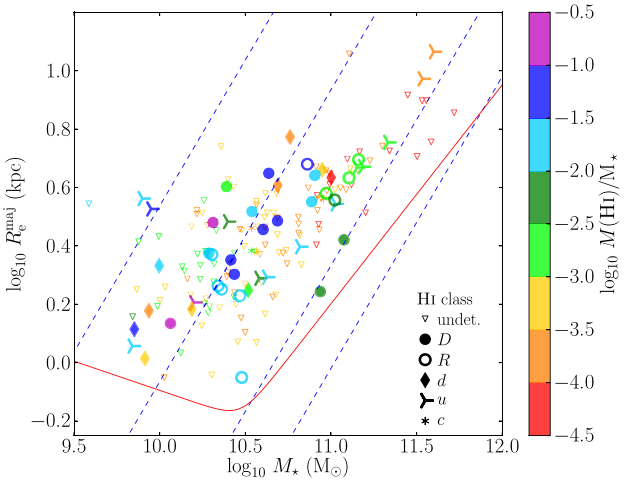

Figure 3. H I properties on the mass–size plane. Different H I morphologies are indicated as in previous figures (see legend on the bottom right) while markers are colour coded according to the $M(\mathrm{H\,I})/M_\star$ value. The velocity dispersion is constant along the blue dashed lines for galaxies following the virial relation ($\sigma_e = 50$, 100, 200 and 300 km s^{-1} from top left to bottom right, respectively; see Cappellari et al. 2006). The red solid line indicates the Zone of Exclusion discussed in Paper XX.

3.4 Diversity of gas accretion histories

The lack of a relation between ETG H I properties (detection rate, mass and morphology) and ETG structure demonstrates the importance of cold gas as an independent probe of the evolution of these objects. Neutral hydrogen observations give us clues about the diversity of ETG assembly histories which are otherwise lost in the relative simplicity of their inner shape and kinematics. Our H I survey demonstrates that there are very diverse evolutionary paths for FRs, which include the formation of both gas-poor objects (undetected in H I or with very low $M(\mathrm{H\,I})/M_\star$) as well as galaxies with a considerable mass of H I spread over a large area (and therefore with low mean column density; see Paper XIII), but that this diversity is not reflected in the structure of ETGs within the FR family. Furthermore, we find that SRs too can accrete cold gas during their life and that they do so at a similar rate as FRs.

It is important to realize that SRs have a fundamentally different internal structure than FRs despite having similar H I properties (in a statistical sense). This means that the accretion of cold gas has not altered their structure, which remains characterized by a relatively round shape and low specific angular momentum within $\sim 1\,R_e$. In other words, gas accretion has not resulted in the growth of a significant stellar disc component in the central galaxy region. The same might be true for FRs: the H I discs and rings in FRs do not need to be causally related to the stellar discs revealed by integral-field spectroscopy inside $\sim 1\,R_e$, although they might well be in at least some cases. To investigate this aspect in more detail we now turn to the study of the kinematical misalignment between H I and stars in these objects.

4 KINEMATICAL MISALIGNMENT BETWEEN H I AND STARS

In order to study the kinematical misalignment between H I and stars we define a sample made of all galaxies for which we can reliably measure the position angle (PA) of the H I kinematical major axis, PA(H I). This includes all galaxies in the *D*, *R* and *d* classes plus two objects hosting H I on an overall unsettled configuration (*u*) but where some of the gas shows ordered rotation – NGC 1023 and NGC 4026. The total sample studied in this section includes therefore 36 ETGs.

4.1 Polar, corotating, counterrotating and warped H I

Fig. 4 shows H I images (from Paper XIII), H I velocity fields (shown for the first time here) and stellar velocity fields (already shown in Paper II) of all *D*, *R* and *u* objects in this sample (26 objects in total; the 10 galaxies classified as *d* are analysed separately below). The figure reveals a diversity of H I stars misalignments, including corotating, polar and counterrotating gas distributions. In a number of cases the strong variation of PA(H I) with radius indicates the warping of the gas disc.

More quantitatively, we derive PA(H I) as a function of radius from the H I velocity field using the KINEMETRY software (Krajnović et al. 2006). In order to maximize the radius out to which PA(H I) can be measured we lower the default minimum coverage of an ellipse with data points to 30 per cent. As we are only interested in the PA values this is an acceptable choice. We compare PA(H I) to the PA of the stellar kinematical major axis, PA(stars), which is given in Paper II. Before proceeding we highlight two aspects which should be kept in mind in order to interpret the results of this analysis correctly.

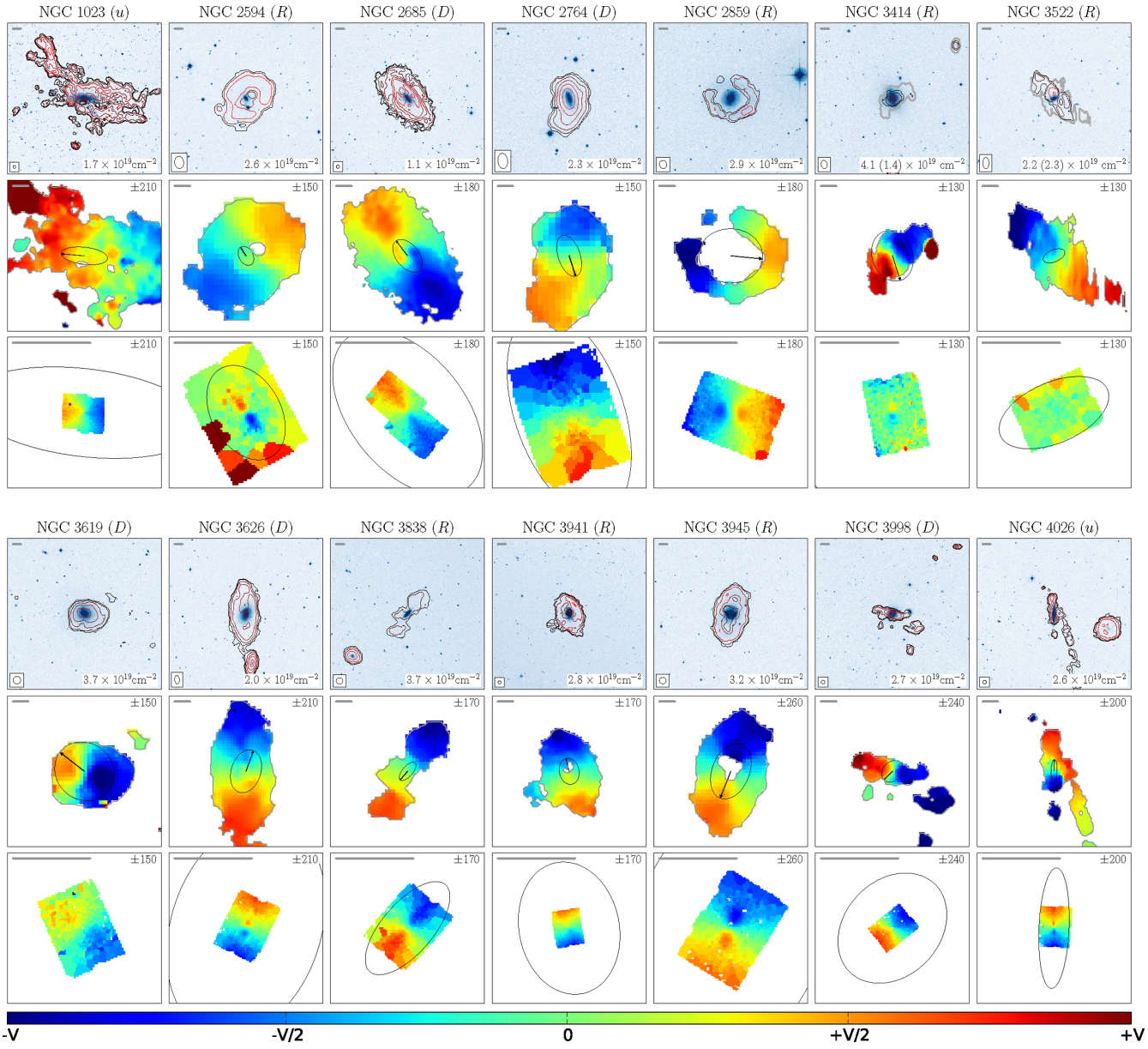

Figure 4. From top to bottom (three panels per galaxy), H I images (100×100 kpc^2), H I velocity fields (50×50 kpc^2) and stellar velocity fields (10×10 kpc^2) of all *D* and *R* ETGs, plus the two *u*'s showing some ordered rotation (NGC 1023 and NGC 4026). The grey scale-bar represents 5 kpc in all figures. The black ellipses overlaid on all velocity fields have semimajor axis equal to $3\,R_e$ and ellipticity taken from Paper II. The black arrow overlaid on the H I velocity fields indicates the PA of the stellar kinematical major axis (receding side) from Paper II and scales with the size of the ellipse. In a few cases the stellar kinematical PA could not be determined reliably and no arrow is shown (see the text). For all velocity fields the velocity range is indicated on the top right. This is kept fixed for the stellar and H I velocity field of a same galaxy in order to enable a comparison of the relative line-of-sight rotation amplitude. The colour scheme of the velocity fields is represented by the horizontal colour bar at the bottom of the figure.

First, while PA(H I) is a function of radius and can be measured sometimes out to tens of R_e, PA(stars) is an average value measured over an aperture of typically $\sim 1\,R_e$ (see Paper II for a detailed discussion). Therefore, we are not comparing the H I kinematics to the stellar kinematics at the same radius, but the H I kinematics (out to large radius) to the inner stellar kinematics. A comparison to the stellar kinematics at larger radius would require deeper optical spectroscopy over a larger field (e.g. Proctor et al. 2009; Weijmans et al. 2009; Arnold et al. 2011, 2013) or the study of planetary nebulae (e.g. Romanowsky et al. 2003; Coccato et al. 2009; Cortesi et al. 2013) or globular cluster kinematics (e.g. Pota et al. 2013; Kartha et al. 2014). A comparison between gas and stellar kinematics at a common, small radius is presented in Paper X using ionized and molecular gas data.

Secondly, while PA(stars) is a well-defined quantity for FRs, where it is typically constant within the observed field, its interpretation may be ambiguous in SRs, where the stellar kinematics is more complex or characterized by very low level rotation. The SRs for which we can measure PA(H I) are NGC 3414, NGC 3522, NGC 5631 (all KDCs) and UGC 03960 ($b_\star$). In the case of NGC 3414 PA(stars) reflects the kinematics of the region outside (and counterrotating relative to) the KDC. To obtain the PA of the KDC one would have to subtract 180° from the value given in Paper II. On the contrary, in NGC 5631 PA(stars) represents the inner (i.e. the

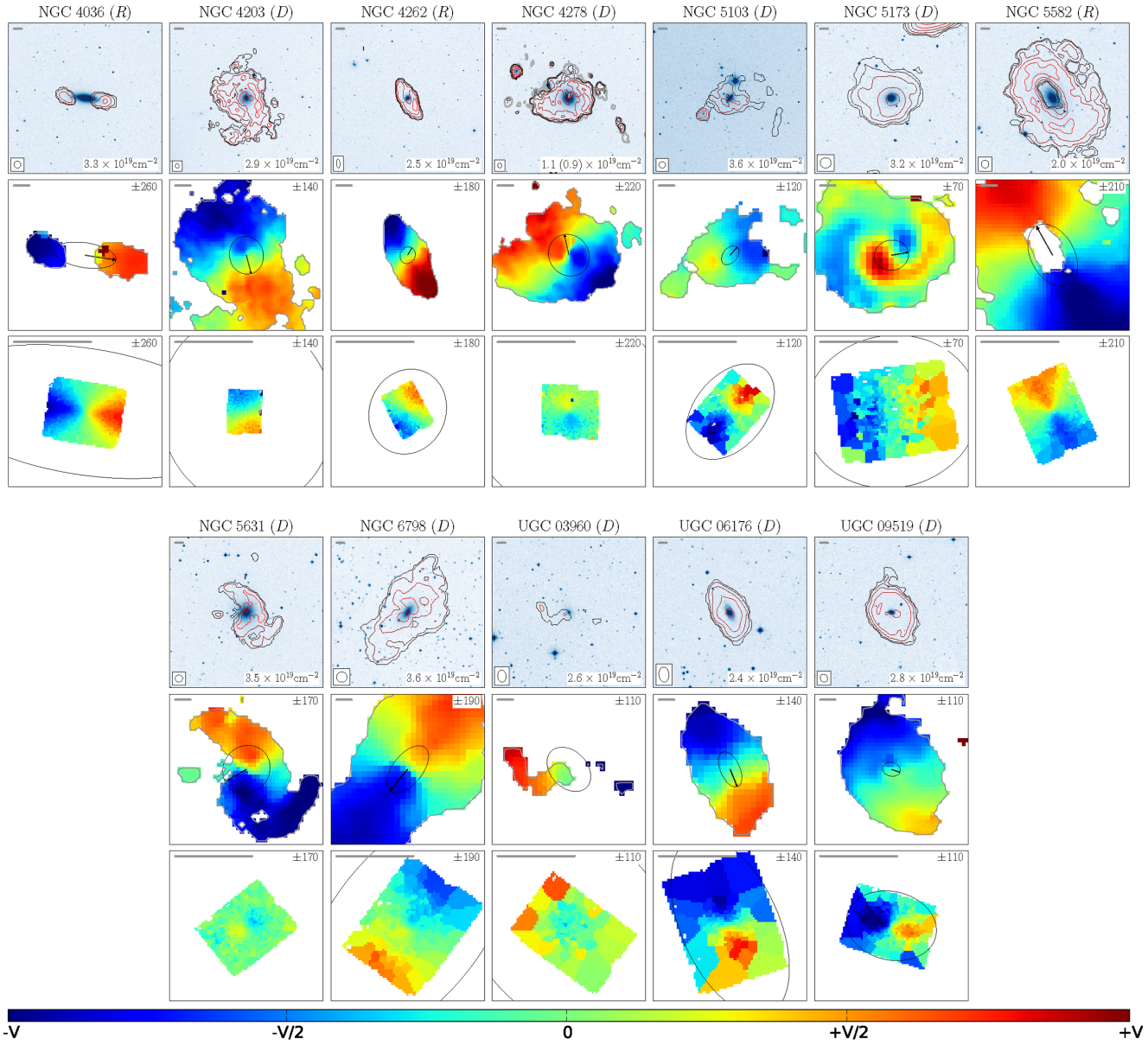

Figure 4 – *continued*

KDC's) stellar rotation. In NGC 3522 the error on PA(stars) is very large because of the overall low-level rotation. In this case we calculate the misalignment relative to the photometric major axis, which coincides with the (uncertain) kinematical one. Similarly, PA(stars) is unconstrained in UGC 03960 and we adopt the photometric PA as a reference. Note that using the photometric rather than kinematical PA would make no difference for NGC 3414, while NGC 5631 is nearly round on the sky and kinematics is the only possible choice.

In Fig. A1 we show PA(H I) − PA(stars) as a function of radius for all 26 galaxies in this subsample. This figure and Fig. 4 show that ∼30 per cent of the systems host corotating H I (NGC 2859, NGC 3838, NGC 3945, NGC 4026, NGC 4036, NGC 4203, NGC 5582 and UGC 06176), while counterrotating and polar H I distributions account each for ∼10 per cent of the sample (NGC 3626, NGC 3941 and NGC 6798 in the first group, NGC 2594, NGC 3998 and NGC 4262 in the second). Note however that the observed misalignment of polar systems depends on viewing angle and it is likely that the H I is on a polar configuration in a larger fraction of all ETGs (e.g. NGC 3619, NGC 5103 and UGC 09519). In most of the remaining systems the misalignment angle varies significantly with radius, indicating the presence of a warp. In the two most extreme cases the H I changes from polar to corotating (NGC 2685) and from counter- to corotating (NGC 5173) with increasing radius.

The situation is somewhat different for *d*s. The H I in these objects is typically very faint and extends over only a couple of Westerbork beams. For this reason instead of using KINEMETRY we assume that PA(H I) does not vary with radius and determine its value by direct analysis of the H I cubes. Position–velocity diagrams along the adopted H I kinematical major axes are published in Paper XIII (their fig. 5). We find that most (8/10) of the *d*s are corotating. The exceptions are one counterrotator (NGC 3032) and one polar system (NGC 3499), as discussed in that paper.

Considering all 36 galaxies together we find therefore that in ∼45 per cent of all ETGs with an H I disc or ring the gas (which can spread out to tens of R_e) is corotating with the stars inside ∼1 R_e. These galaxies are all FRs where the gas accretion episode traced

by the H I might be related to the formation of the stellar disc. They are in many respects similar to spiral galaxies as they host cold gas and stars corotating on the same disc – the only difference being the absence of bright, star-forming spiral arms owing to the low-H I column density (Paper XIII).

The remaining 55 per cent of this sample is composed of ∼10 per cent of counterrotating H I systems, ∼10 per cent of polar objects and ∼35 per cent of ETGs with a complex, warped H I distribution, some of which may in fact be polar. The link between H I disc and stellar disc in these objects is less obvious.

These results show that the existence of multiple kinematical subcomponents in ETGs, well documented in their inner region for the stellar and ionized-gas phases, holds also on much larger scales. Following our results on the fraction of ETGs with a kpc-scale KDC (∼7 per cent including counterrotating cases; Paper II) and misaligned ionized-gas kinematics (∼36 per cent; Paper X, see also Bureau & Chung 2006) we are now finding misaligned H I distributions on scales from a few to tens of kpc in ∼12 per cent of all ETGs (∼15 per cent outside the Virgo cluster; for previous studies of smaller samples of ETGs with misaligned H I see, e.g. van Gorkom, Schechter & Kristian 1987; Bertola, Buson & Zeilinger 1992; Bettoni et al. 2001).

Whether or not associated with the presence of a stellar disc, the H I detected in ETGs provides important clues on the origin of the cold interstellar medium detected in the inner region of these objects in the form of ionized and molecular gas. This is clear in Fig. A1, where we show at $R = 0$ the data point corresponding to the ionized-gas kinematics (when detected), which was already found to be invariably aligned with the CO kinematics (Paper X). The figure confirms previous claims that H I, H_2 and ionized gas share the same kinematics in the region where they overlap (Morganti et al. 2006 Paper X). The few exceptions are NGC 1023, NGC 3414, NGC 4278, NGC 5103 and NGC 5631. The first hosts an unsettled gas distribution with very complex gas kinematics, and it is unlikely that the central value of PA(H I) derived from the velocity field is representative of the actual inner gas motion. Furthermore, Morganti et al. (2006) show that in both NGC 3414 and NGC 4278 the ionized-gas velocity field twists in such a way that the outer ionized-gas kinematics is aligned with the inner H I kinematics. The same occurs in NGC 5631. Therefore, these three galaxies conform to the general rule too. We do not have a good explanation for the misalignment between H I and ionized gas in NGC 5103, which represents the only genuine exception to the rule. Not shown in Fig. A1, *d* galaxies contribute to strengthening this result. The H I is always corotating with the CO and ionized gas, including the two cases where the H I is misaligned relative to the stars (NGC 3032 and NGC 3499).

4.2 Misalignment in fast and slow rotators

Fig. 5 summarizes our findings by showing all H I misalignments on the $M(\mathrm{H\,I})/M_\star$ versus $\lambda_R/(0.31\sqrt{\epsilon})$ plane of Fig. 2. For each galaxy we adopt here the median misalignment value measured from the radial profile shown in Fig. A1. The median value is a fair representation of the overall misalignment for all galaxies except the heavily warped NGC 2685 and NGC 5173, which we highlight in the figure. On the one hand Fig. 5 shows a significant population of FRs where H I and stars are kinematically aligned (dark blue symbols, with the just mentioned exception of NGC 2685 and NGC 5173). In these galaxies gas and stars are just two different but coupled components of the same disc. On the other hand, as already emphasized above, the H I discs and rings detected in FRs are not always associated with the inner stellar disc, not even for the flattest and fastest rotators (see for example NGC 3626, NGC 5103 and UGC 09519). In many FRs the large-scale H I kinematics is obviously not a continuation of the inner stellar kinematics to larger radius. On the contrary, counterrotating and polar H I distributions account for exactly 1/4 of all FRs analysed in this section, while another 1/4 consists of warped discs. The detected H I is therefore aligned with the inner stellar disc only in half of the cases. Neutral hydrogen observations show therefore that FRs, while being a dynamically simple and homogeneous family inside $\sim 1\,R_e$, are much more complex and diverse in their outer regions, in agreement with results obtained using other kinematical tracers at large radius (e.g. Coccato et al. 2009; Pota et al. 2013).

The other clear result is that in none of the four SRs the H I kinematics is aligned with the stellar kinematics or morphology. In fact, all these systems exhibit a (close to) polar H I distribution, although PA(H I) typically varies with radius (Fig. A1). We also note that the H I morphology of these systems, although disc- or ring-like, appears disturbed (Fig. 4), with some cases intermediate between a *D*/*R* and a *u* classification. The lack of very regular, settled H I discs/rings in SRs and the prevalence of polar systems may be the only difference from the FR family (H I wise), although even among FRs many gas discs and rings appear disturbed or not perfectly settled (e.g. NGC 2764, NGC 3998, NGC 4203, NGC 4278 and NGC 5103). A larger sample of H I-rich SRs would be needed to confirm this indication.

The above results, together with the established weak relation between $M(\mathrm{H\,I})$ and ETG luminosity (e.g. Knapp et al. 1985; Wardle & Knapp 1986, Paper XIII), confirm the severe disconnect between ETG H I properties and their stellar component. They show, as argued in Section 3.4, that H I provides clues about the complex evolution of ETGs which would go unnoticed using only other observables. Confirming this complexity, we also find that the H I kinematical misalignment does not depend in any clear way on ETG stellar mass, environment density (quantified in Paper VII) or H I mass. For example among the very H I-rich galaxies in poor environments we find NGC 5582 (corotating *R*), NGC 6798 (counterrotating *D*) and UGC 09519 (warped *D*). Low-mass, isolated galaxies include NGC 2594 (polar *R*), UGC 06176 (aligned *D*) and again UGC 09519. Among the massive ETGs we find relatively small, aligned H I discs/rings as in NGC 2859 and NGC 4036 but also (close to) polar H I as in NGC 3414 and NGC 5631, and the warped *D* NGC 4278. The only exception is that the lowest $M(\mathrm{H\,I})$ systems are all *d*s (Paper XIII) and, as illustrated above, mostly kinematically aligned to the stellar rotation. There is of course some dependence of H I properties on ETG mass and environment across the entire ATLAS^{3D} sample. This is discussed in detail in Paper XIII, where we show that unsettled H I distributions become more common, and the typical H I mass decreases, as environment density and galaxy mass increase. Here we find that there is no additional trend with environment and stellar mass when studying the kinematical misalignment of settled H I discs.

Ever since the work of Knapp et al. (1985) this decoupling between stars and H I in ETGs has been attributed to the external origin of the H I. The main point of this interpretation is that most of the present-day gas must be accreted once the formation of the (inner region of the) host ETG is basically complete. The accreted gas could come from the intergalactic medium or be brought in by small gas-rich satellites which individually do not contribute significantly to the stellar mass of the ETG but may bring a significant addition to its interstellar medium. In fact, even when gas is acquired at the same time as the formation of the stellar body, e.g. in gas-rich

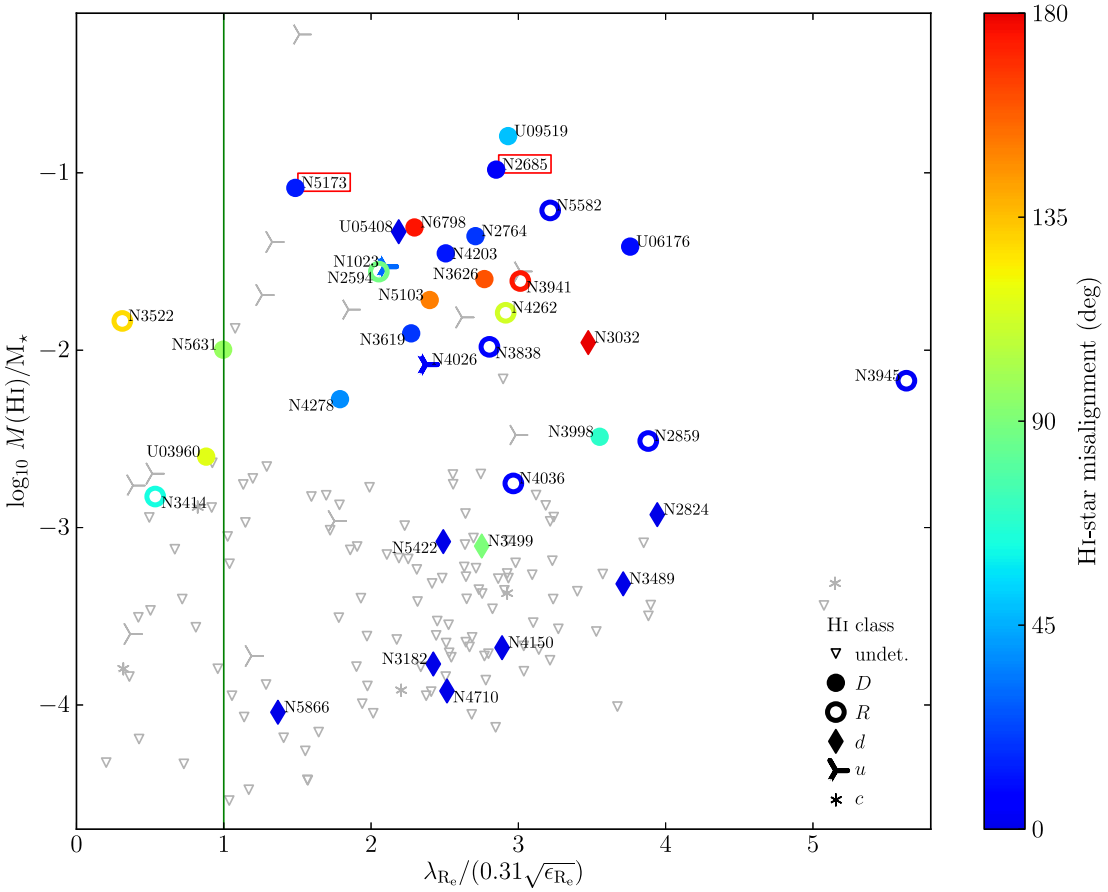

Figure 5. H I kinematical misalignment on the $M(\mathrm{H\,I})/M_\star$ versus $\lambda_R/(0.31\sqrt{\epsilon})$ plane. This figure is the same as Fig. 2 but here we highlight only the 36 galaxies for which we are able to study the H I kinematical misalignment (see Section 4 for details on this subsample; the remaining galaxies are shown with light grey markers). We colour code them according to the median misalignment angle calculated over the full radial extent of the H I disc or ring. See Fig. A1 for the variation of the misalignment angle as a function of radius in individual galaxies. Note that NGC 2685 and NGC 5173, the two most heavily warped H I systems in the sample, have a small median misalignment angle which is not representative of their true complexity. For this reason we highlight them here with a red box.

major mergers, there does not need to be a strong coupling between the stellar body of the remnant and the larger scale H I distribution. Merging and accretion events are expected to occur in a ΛCDM Universe, where galaxies grow hierarchically, and our results may be seen as a confirmation of these theories. Qualitative statements of this kind have been made by previous authors and, at this stage, do not represent an advancement in our understanding of ETG formation. For this reason we attempt to take a step forward and perform a quantitative comparison to galaxy formation simulations in the next section.

5 COMPARISON TO COSMOLOGICAL SIMULATIONS

We compare ETGs in the ATLAS^{3D} sample to galaxies formed in two sets of hydrodynamical simulations performed by Oser et al. (2010) and Hirschmann et al. (2013). These are high-resolution re-simulations of ∼50 dark matter haloes extracted from a large, ΛCDM, dark-matter-only simulation. In each re-simulation baryonic processes such as hydrogen and helium cooling, star formation and supernova feedback are implemented in the presence of a uniform UV background. The two sets of simulations have different implementations of supernova feedback. In the first set the feedback is purely thermal (hereafter, NoW simulations because they do not include galactic stellar winds). These are the simulations analysed by Paper XXV to study the generic formation paths of SRs and FRs in a cosmological context. Simulations in the second set start from identical initial conditions but include an additional empirical model for galactic outflows driven by winds from star-forming regions (Oppenheimer & Davé 2006; we will refer to these as W simulations). All details on the galactic wind implementation and a comparison of galaxy properties between the two models are presented in Hirschmann et al. (2013). Here we study for the first time the distribution and kinematics of cold gas in the simulations. As we will show, these two sets give profoundly different predictions for galaxies' H I properties. We refer to Oser et al. (2010) and Hirschmann et al. (2013) for a full description of the simulations.

For the purpose of this work it is important to first investigate whether the simulated galaxies are a reasonable match to the ETGs we want to compare them to. On the one hand, they cover the same $M_\star$ range (from $\sim 10^{10}$ to a few times 10^{11} $M_\odot$). Furthermore, the NoW simulations are in reasonable agreement with the observed mass–size relation of ETGs (Oser et al. 2012) and exhibit a diversity of stellar kinematical properties similar to that of real ETGs (Paper XXV). On the other hand, not all simulated galaxies, in particular the W sample, would necessarily meet the morphological selection of the ATLAS^{3D} sample, which requires the absence of large-scale spiral arms in a galaxy optical image (Paper I). This is

essentially a selection against strong star formation on a disc while about half of all simulated galaxies have relatively large specific star formation rate ($>10^{-11}$ yr^{-1}) at $z = 0$. Similar values are measured in only a handful of the observed ETGs (Davis et al. 2014). We note however that the uncertainty on the simulated star formation rate is large because of uncertainties in, e.g. star formation and feedback physics and their actual implementation. Additionally, neither of the simulated samples include active galactic nuclei, which could be an efficient way to suppress star formation. Therefore, we decide not to exclude star-forming galaxies from the comparison. Instead, we highlight this as a caveat of this work and stress that more sophisticated simulations would be needed to fully replicate the ATLAS^{3D} selection.

The simulations do not include a full treatment of different gas phases and the correspondence between simulated gas particles and H I is not obvious. As a first step we define cold gas following the criterion of Hirschmann et al. (2012), which is based on a selection of gas particles on the density–temperature plane. This is preferred to a simple temperature selection since dense star-forming gas (which we want to include in the cold-gas budget) can be relatively hot in the NoW simulations. Additionally, we assume that this cold gas is made of two phases, atomic and molecular (ignoring that some of it may in fact be ionized). We separate the two phases on the gas' face-on view by applying equation 39 of Krumholz, McKee & Tumlinson (2009). In their equation s is the H I+H_2 column density in $M_\odot$ pc^{-2} (see Schruba et al. 2011 for a comparison between this theoretical relation and observations). This results in a relatively sharp transition from an atomic- to a molecular-dominated regime at a total gas column density of $\sim$10 $M_\odot$ pc^{-2} (Wong & Blitz 2002; Bigiel et al. 2008). The resulting face-on H I images are used to calculate H I mass and column density distribution for all simulated galaxies (at the typical gas resolution of $\lesssim$0.5 kpc).

In order to study the morphology and kinematics of the H I we construct seven different projections of each simulated galaxy relative to an hypothetical observer: face-on (relative to the stellar kinematics); rotated by 30°, 60° and 90°, respectively, about the stellar morphological major axis in the face-on view; and rotated by 30°, 60° and 90°, respectively, about the stellar morphological minor axis in the face-on view. When constructing these projections we do not separate H I from H_2 as Krumholz's prescription is strictly valid only when the gas is seen face-on. This does not affect our conclusions since we are mainly concerned with the kinematics of the gas, which is the same for all cold-gas phases.

All gas mass and surface density calculations as well the analysis of the H I and stellar kinematics presented below are performed after removal of star and gas particles associated with satellite dark matter subhaloes according to the SUBFIND algorithm of Springel, Yoshida & White (2001). Furthermore, we exclude from the calculation of gas mass and surface density the discrete cold gas clouds which are a known artefact of smoothed particle hydrodynamics simulations and which are not part of the gas discs we wish to study (Sijacki et al. 2012). These clouds, visible in some of the images discussed in Section 5.1, have a typical mass above 10^7 $M_\odot$ and may therefore have a significant impact on the value of M(H I) if included in the calculation.

Before showing the result of the comparison between simulated and real ETGs we note that the ATLAS^{3D} sample is volume limited and complete down to $M_K = -21.5$ mag (Paper I). On the contrary, the sample of simulated galaxies is not volume limited (it is a set of individual simulations rather than a single, large simulated volume) and does not follow the observed galaxy luminosity function. Therefore, we cannot compare the statistical distribution of real and simulated galaxy properties. Instead, we investigate whether the diversity of ETG H I properties is reproduced by the simulations.

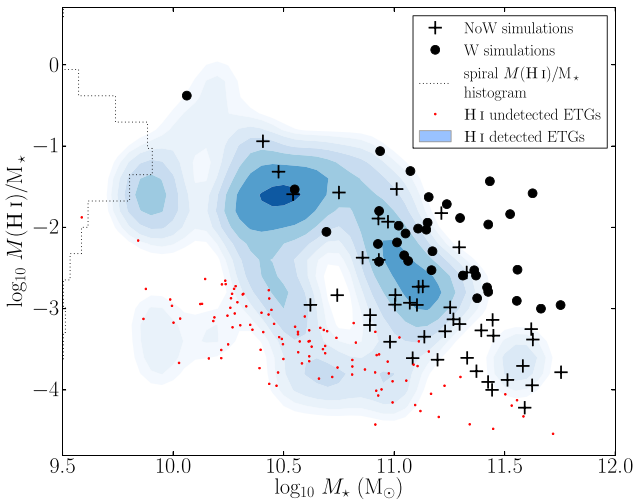

Figure 6. M(H I)/$M_\star$ plotted against $M_\star$ for simulated galaxies (black circles and crosses) and real ETGs from Paper XIII. For the latter, the blue area shows the kernel density estimate derived using all 53 galaxies with detected H I while the red dots indicate H I non-detections and are therefore upper limits on M(H I)/$M_\star$. The dotted histogram along the vertical axis represents the M(H I)/$M_\star$ distribution of spiral galaxies derived as explained in the text.

5.1 H I mass and morphology

The first step of our comparison is presented in Fig. 6, where we plot M(H I)/$M_\star$ against $M_\star$ for galaxies in the two sets of simulations. Stellar mass values are taken from Paper XXV for the NoW simulations and are measured in an identical way for the W simulations. For comparison we show the distribution of real ETGs distinguishing between H I detections (blue density field) and non-detections (red dots). We also show the M(H I)/$M_\star$ histogram of spiral galaxies. This is obtained from the M(H I)/L_K histogram shown in Paper XIII assuming that for $M_\star > 10^{10}$ $M_\odot$ the typical spiral has $M_\star/L_K = 0.8$ $M_\odot/L_\odot$ (Bell et al. 2003).

The figure shows that the NoW simulations produce galaxies whose H I content is to first order comparable to that of real ETGs and lower than that of spirals. The main discrepancy between NoW simulated and real ETGs is that extremely gas-poor galaxies with M(H I)/$M_\star$ below a few times 10^{-4} are underrepresented in the simulations. This results in an overall smaller range of M(H I)/$M_\star$ at any given $M_\star$ compared to the observations. Nevertheless, both the fact that such range is large in the simulations and that the typical M(H I)/$M_\star$ decreases with $M_\star$ (above a stellar mass of $\sim 5 \times 10^{10}$ $M_\odot$) are important points of agreement with the observed ETG sample.

The situation is different for the W simulations. These galaxies are typically gas richer than NoW ones (Hirschmann et al. 2013). They populate the high-M(H I)/$M_\star$ end of the observed ETG distribution. At $M_\star > 10^{11}$ $M_\odot$ we find a number of objects whose H I content is too large by a factor of 10 to 100 compared to the data. We conclude that W systems are, as a family, too H I rich and that NoW galaxies are a better (albeit not perfect) match to real ETGs in terms of H I mass.

Having established this we can now analyse the H I morphology of the simulated galaxies. We show three examples in Fig. 7 and

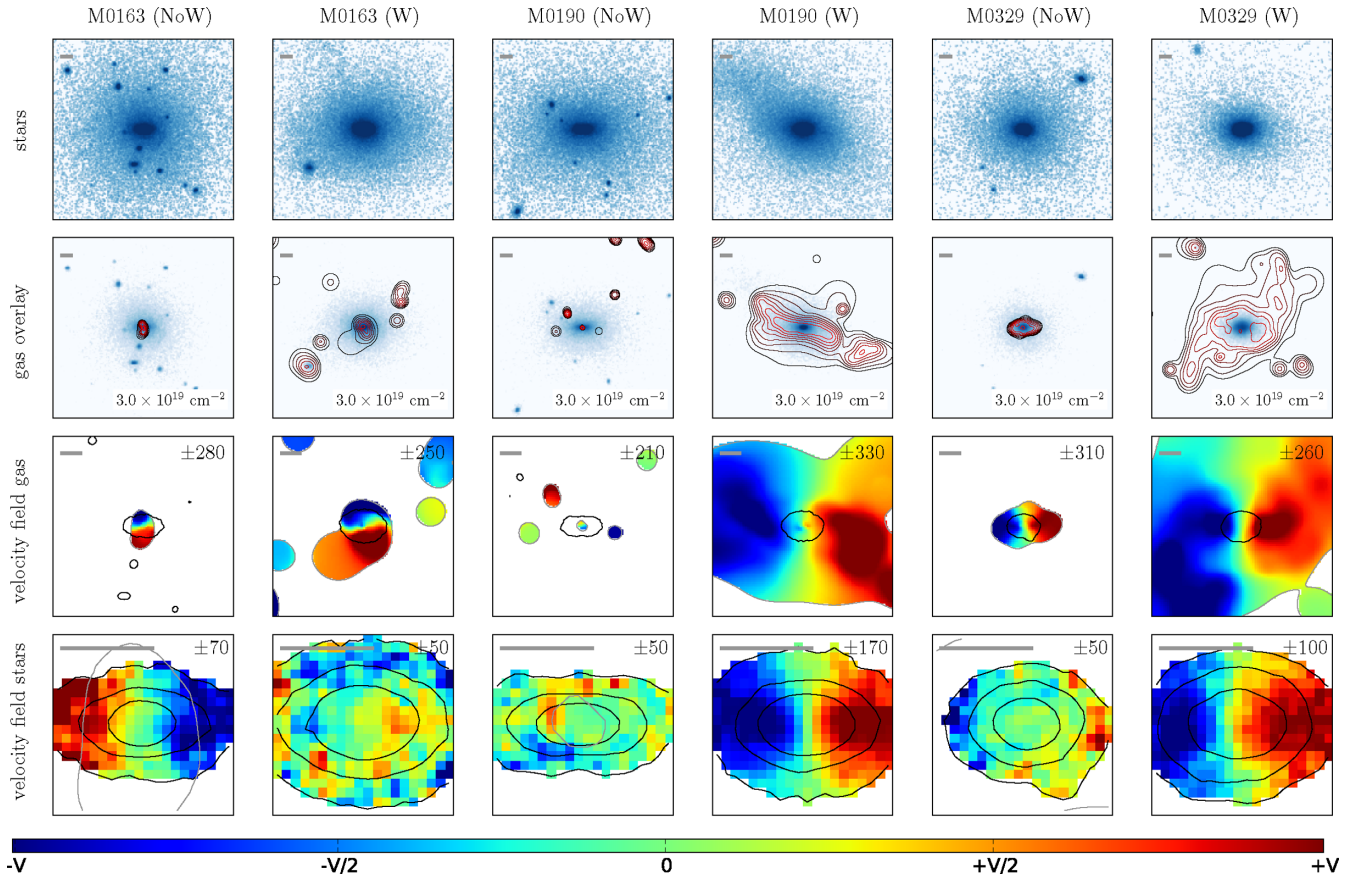

Figure 7. Three examples of simulated galaxies. For each galaxy we show the result of the NoW and the W simulation next to each other to highlight their differences. Each column represents one simulated object – four rows per galaxy – viewed at an inclination of 60°. The first row corresponds to an extremely deep optical image (∼29 mag arcsec^{-2} in *V* band). The remaining rows are equivalent to those shown in Fig. 4 for real ETGs. Namely, the second row corresponds to a SDSS-like optical image with H I contours overlaid; the third row shows the intensity-weighted H I velocity field; the last row shows the intensity-weighted stellar velocity field. The linear scale of the various panels is the same as in Fig. 4, with the grey scale-bar representing 5 kpc. Galaxies are sorted according to decreasing dark matter halo mass (left to right). The outer stellar isophote corresponds to a stellar mass surface density of 500 $M_\odot$ pc^{-2}. The colour scheme of the velocity fields is represented by the horizontal colour bar at the bottom of the figure.

another three in Fig. 8. For each galaxy we show the NoW and the W simulation next to each other. These images and velocity fields are immediately comparable to those in Fig. 4 and are drawn adopting the same linear scale and gas contour levels. The only difference between observed and simulated galaxy figures is that for the latter we also show the equivalent of a deep optical image (top panel, see figure caption).

Figs 7 and 8 are meant to show a few cases representative of the diversity of galaxies produced by the simulations as well as the difference between the NoW and W simulation for a same halo. Indeed, it is immediately obvious that changing the star formation feedback implementation has a strong impact on the properties of a simulated galaxy. The same object can be a FR in the NoW simulation and a SR in the W one (M0163) or vice versa (M0190, M0329). Furthermore, it can be surrounded by a large gas distribution in the W simulation but have the gas disc entirely confined inside the stellar body in the NoW simulation (e.g. M0190, M0721). In fact, the larger size of the H I distribution in the W simulations is a general result valid for all galaxies and a consequence of the mechanical nature of the W feedback, which pushes gas to large radius while keeping it cold. A visual comparison between Fig. 4 and Figs 7 and 8 shows that these large W gas discs match reasonably well the size of the H I discs and rings in gas-rich ETGs. They too, like the observed systems, exhibit slight warps in the outer regions, possibly owing to their large size. The NoW gas distributions are on the contrary too small.

The fact that the NoW simulations are a better match to the observed ETG M(H I) distribution (Fig. 6) but that W objects are a better match to the observed size of the H I discs may seem contradictory. In fact, this is easily understood noting that in all simulations the H I column density is on average higher than observed. For this reason H I discs with the right mass are too small (NoW) and H I discs with the right size are too massive (W). This result, which is clear from a comparison of the H I contours in Fig. 4 with those in Figs 7 and 8, is shown more quantitatively in Fig. 9. In this figure the black lines represent the H I column density distribution in simulated galaxies while the red solid line shows the distribution in real galaxies (represented by the best-fitting Schechter function derived in Paper XIII). This mismatch is consistent with the fact that simulated galaxies appear to be forming stars at a rate higher than real ETGs at $z = 0$ (Hirschmann et al. 2013).

Although not the focus of this study, it is worth noting in this context that all simulated galaxies host cold gas above a column density of 10^{21} cm^{-2}. This gas, which we do not include in our calculation of H I mass and column density, is more centrally concentrated than the H I and can be related to the molecular gas found in the central region of ETGs (Paper IV). Its mass is typically between 5×10^7 and 5×10^9 $M_\odot$ with a handful of exceptions at lower mass and

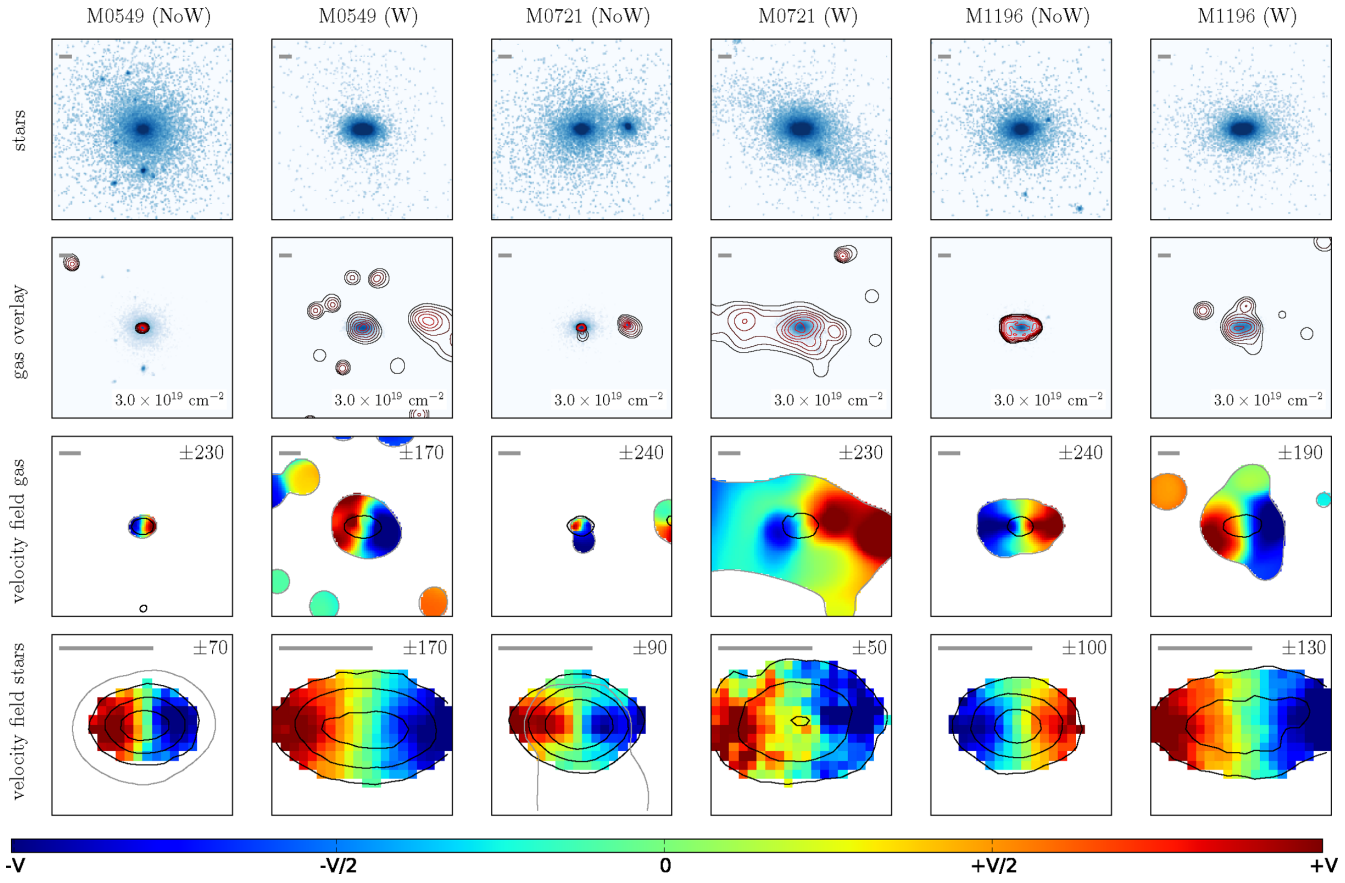

Figure 8. Three more examples of simulated galaxies. See caption of Fig. 7.

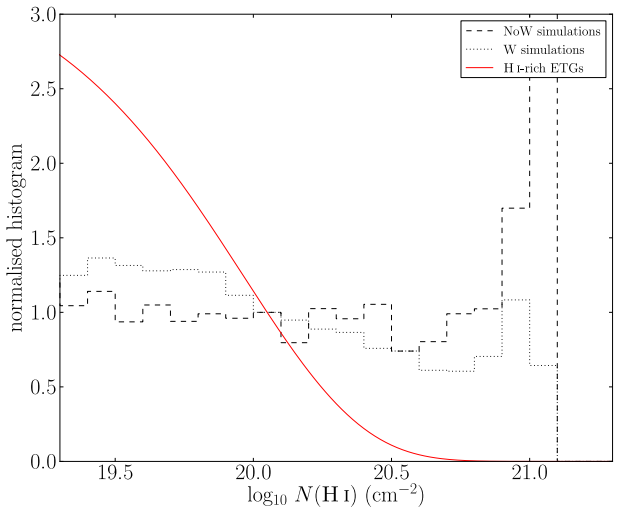

Figure 9. H I column density distribution in the simulations compared to that in real ETGs. The latter is represented by the best-fitting Schechter function derived in Paper XIII. For both NoW and W simulations we plot the median of the normalized distributions of all individual galaxies. The distributions are obtained for the cold-gas face-on view. Both median distributions and the Schechter function are scaled to intersect at $N(\mathrm{H\,I}) \sim 10^{20}$ cm^{-2}. The peak at (and sharp drop after) $N(\mathrm{H\,I}) = 10^{21}$ cm^{-2} is due to our definition of H I in the simulations (see the text). This effect is more pronounced in the NoW case because the distribution of total gas surface density extends to larger values than in the W simulations.

no significant difference between NoW and W simulations. Both sets of simulations miss therefore the large population of ETGs with $M(\mathrm{H_2}) < 5 \times 10^7$ M$_\odot$ reported in Paper IV while on the gas-rich side of the distribution the molecular gas masses are in reasonable agreement with the observations. We find that the molecular-to-total cold-gas fraction is larger in the NoW than in the W simulations. This is a consequence of their higher average cold-gas column density coupled with our method for separating atomic from molecular gas.

5.2 H I discs and misalignment in simulated fast and slow rotators

Figs 7 and 8 show that not only the H I mass and morphology but also the gas kinematical misalignment is affected by the feedback implementation. For example, M0549 hosts a small counterrotating gas disc in the NoW simulation and a large, corotating one in the W simulation; M0721 hosts a small corotating disc in the NoW simulation and a very large, counterrotating one in the W simulation. This kind of difference between the H I misalignment of NoW and W galaxies is very common within the sample of simulations analysed here. It is caused by the cumulative effect of galactic stellar winds on a galaxy and the satellites which it accretes as the simulation progresses.

Taken together, the NoW and the W simulations seem to reproduce qualitatively the large variety of gas morphologies and kinematics of real H I-rich ETGs. In this sense it is useful to associate some of the examples in Figs 7 and 8 to ETGs in the ATLAS^{3D} sample. Bearing in mind that these matches are not exact and may not hold at a more quantitative level (as we illustrate below),

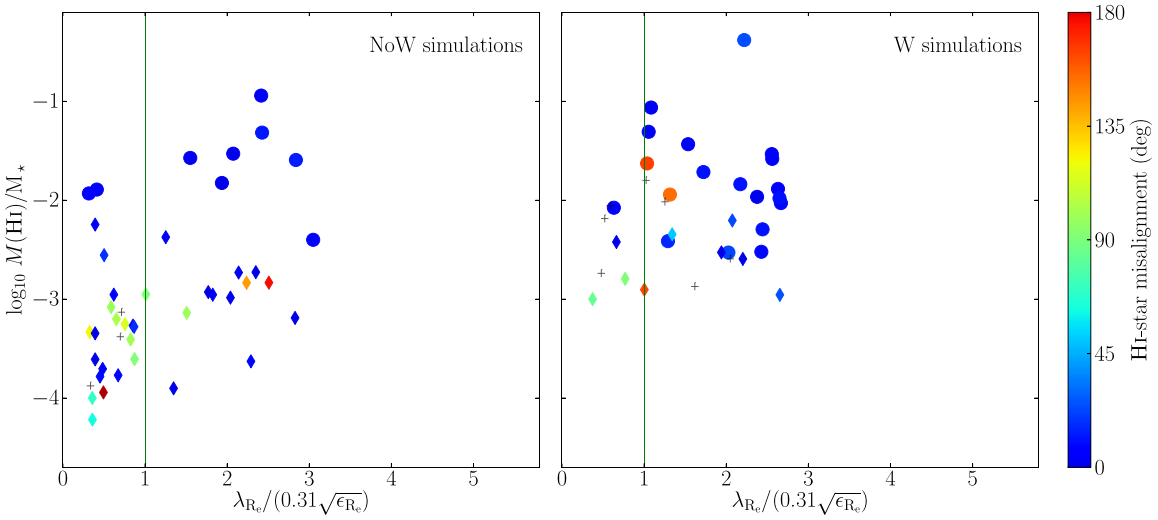

Figure 10. H I kinematical misalignment of the simulated galaxies on the $M(\mathrm{H\,I})/M_\star$ versus $\lambda_R/(0.31\sqrt{\epsilon})$ diagram. We show NoW simulations in the left-hand panel and W simulations in the right-hand panel. The small grey crosses indicate simulations where the gas is not settled and therefore we do not measure the misalignment angle. See the caption of Fig. 5 for more details on the figure. Note that we show these figures with the same axes limits as in Fig. 5 to facilitate the comparison between simulated and real galaxies.

M0163-NoW is for example a FR with a small polar gas disc which may be related to NGC 3499. M0163-W, a bright SR with a polar gas disc slightly larger than the stellar body, could be compared to NGC 3414. M0549-NoW hosts a small, counterrotating gas disc similar to NGC 3032. M1196-NoW and many W galaxies (e.g. M0190, M1196) represent cases of large, corotating H I discs around FRs (similar, for example, to NGC 5582 and NGC 3838). M0329-W exhibits an H I warp and tails comparable to those of NGC 4278. Counterrotating gas discs around FRs (e.g. NGC 6798) can be associated with M0721-W. The same galaxy simulated with the NoW feedback shows a small, corotating gas disc similar to the vast majority of the *d* ETGs (e.g. NGC 4710, NGC 4150). This diversity is similar to the observed one and includes also some cases of unsettled H I distributions, as observed (Paper XIII).

Yet, the match between simulations and observations is far from perfect. In addition to the points of friction mentioned above with respect to mass and column density distributions, the ATLAS^{3D} sample includes H I-rich ETGs not represented in the simulations such as SRs (NGC 3522) and FRs (NGC 2594, NGC 3998) with large polar rings. Furthermore, some simulated systems seem to have no corresponding real galaxy, such as the SRs with small, aligned gas discs (e.g. M0329-NoW). These objects may however be related to the SRs with aligned ionized-gas discs discussed in Paper X. This, together with the lack of central H I depressions (or narrow H I rings) in the simulations, is a reminder that a more sophisticated treatment of gas physics may be needed in order to relate simulated to real galaxies.

We conclude this section by comparing simulated and observed misalignments on the $M(\mathrm{H\,I})/M_\star$ versus $\lambda_R/(0.31\sqrt{\epsilon})$ diagram. The complexity of the observed ETG H I properties is summarized in Fig. 5. That figure highlights that H I discs around FRs are very diverse in terms of their kinematical misalignments from the stars. Furthermore, it shows that SRs too can host an H I disc or ring and that this is typically polar relative to the stars. To investigate whether a similar picture emerges from the simulations we construct a figure equivalent to Fig. 5. The basis of this analysis is the simulated stellar and cold-gas velocity fields represented by the examples in Figs 7 and 8, which are obtained on a projection such that the inclination of the stellar body is 60°.

Measurements of PA(stars) are straightforward as nearly all simulated galaxies have their kinematical major axis aligned along the *X*-axis. In order to measure PA(H I) as a function of radius we make use of the ROTCUR task part of the GIPSY package (van der Hulst et al. 1992). This task fits tilted-ring models to a velocity field and is equivalent to the software used for the analysis of real galaxies (see Section 4). In this case, we fix the centre of the rings to the stellar centre of mass and the H I systemic velocity to the stellar value. We then solve for PA(H I), inclination and rotation velocity of all rings. In what follows we analyse PA(H I) only.

We summarize the result of this analysis in Fig. 10, where the values of λ_R and ϵ are measured on the edge-on projection. These values are taken from Paper XXV for the NoW galaxies and are measured in the same way for the W objects. Galaxies with an H I radius smaller than $3\,R_e$ are shown as diamonds. Values of R_e are also taken from Paper XXV and measured in the same way for the W models. The figure shows that, as discussed above, the simulations are able to make H I discs around both FRs and SRs, in agreement with the result of Section 3. As noted above, it is also important that in some of these objects the H I is misaligned (e.g. polar or counterrotating) relative to the stellar kinematics. However, the similarities between simulated and real ETGs on this diagram do not go much further than these qualitative statements.

A first obvious difference is that, compared to Fig. 5, the vast majority of both W and NoW FRs host H I on an aligned configuration. There are a few exceptions including some of the FRs in Figs 7 and 8: M0163-NoW (polar) M0549-NoW (counterrotating) and M0721-W (counterrotating). However, strongly misaligned systems are confined to much lower levels of stellar rotation and gas content compared to some of the observed H I counterrotators (NGC 3626, NGC 3941, NGC 5103 and NGC 6798) and polar rings (NGC 2594 and NGC 3998). In the W simulations the only misaligned FRs lay, in fact, close to the empirical boundary between FRs and SRs. The kinematical alignment between H I and stars in all the other, faster rotating simulated galaxies makes them more

similar to spirals than to real FRs as a family. Such stronger coupling between gas and stars compared to real ETGs may be related to the larger gas surface density and star formation rate in the simulations, as highlighted in Section 5.1.

Rewinding the simulations reveals that the rare cases of large H I misalignment in FRs at $z = 0$ are usually the result of very recent events. For example, M0721-W (Fig. 8) spends most of its life as a FR with aligned H I, until a merger with a relatively small but very gas-rich satellite at $z \sim 0.3$ turns it into an H I counterrotator. The H I tail in Fig. 8 is a remnant of that event. Another example is M0549-NoW (also in Fig. 8). This system is surrounded by a large, warped gas disc for a large fraction of its life. Gas in the inner part of the disc is kinematically aligned with the inner stellar rotation except for some short intervals where it appears to be close to polar. The gas disc mass and size decrease as the galaxy evolves and by $z \sim 0.1$ the disc is so small that a relatively minor gas accretion event results in the current counterrotating H I disc. Similarly, the FR M0163-NoW (Fig. 7) has been hosting a polar gas disc only for the last ∼2 Gyr, and in the past has been both a gas co- and counterrotator. Given that the H I orbital time in ATLAS^{3D} galaxies is at most ∼1 Gyr it is possible that the ETGs with misaligned H I have acquired their gas relatively recently.

On the contrary, FRs with an aligned (although frequently warped) gas disc at $z = 0$ have typically been in such a configuration for most of their life, with occasional periods of time during which the gas is unsettled following a merger. This is true for ∼80 per cent of all NoW FRs and ∼70 per cent of all W FRs. Note that such a persistent alignment between stellar and gas kinematics is not the result of a lack of satellite accretion. On the contrary, these objects experience continuous merging (depending on their halo mass), but their gas disc is probably sufficiently massive at all times to prevent significant misalignments from developing. We do not investigate this aspect in more detail since our focus here is the comparison to observed ETGs at $z = 0$ and not so much a detailed study of why simulated galaxies look the way they do.

Slightly different paths for the formation of an aligned FR are possible (although less frequent) in the simulations. For example, M0721-NoW is a SR with very low level rotation and a counter-rotating gas disc at $z \sim 1$. This gas lives relatively undisturbed for the next ∼2 Gyr and during this time forms a number of new stars sufficient to change the direction of net rotation of the stellar body and to turn the object into a FR. So this is a case where rather than the gas disc changing its kinematics following gas accretion, it is the stellar body that changes its kinematics following star formation. Whether such evolutionary paths occur also in the real Universe remains to be established.

The other, already mentioned difference between Figs 5 and 10 is the existence of simulated gas-rich SRs where the H I is co- or counterrotating relative to the stars. These SRs have no counterpart in the ATLAS^{3D} H I sample but may be related to the ionized-gas SR corotators of Paper X. Rewinding the simulations reveals that many of the SRs with a small corotating disc at $z = 0$ used to have a polar disc (or sometimes a counterrotating one), which has settled only recently on an aligned configuration. As noted above for the misaligned FRs, the H I kinematical misalignment can change very frequently in the simulations, mostly following merging with satellites. Polar gas distributions like the observed ones are found too (e.g. M0163) but they are not the rule. Their history too includes frequent changes of the kinematical misalignment as a result of mergers.

The comparison presented in this section indicates that simulations are only partially successful at reproducing the observed H I properties of ETGs. A careful treatment of gas physics is essential and it appears that a better match to the observations needs to be achieved before ΛCDM simulations can teach us why and how ETGs evolve into the diverse (H I-wise) family they are today.

6 SUMMARY

In a previous ATLAS^{3D} paper (Paper XIII) we demonstrate on a strong statistical basis that a large fraction of all ETGs outside the cluster environment host a significant mass of H I gas. In particular, 1/4 of all ETGs outside the Virgo cluster host a disc or ring of low-column-density H I with size from a few to tens of kpc, and mass from $\sim 10^7$ to a few times 10^9 $M_\odot$. Here we investigate the link between the H I properties (mass and morphology) of these galaxies and their internal structure. The latter is determined on the basis of galaxies' optical morphology and stellar kinematics, leading to their classification as SRs or FRs. Furthermore, we study the kinematical misalignment between H I (out to large radius) and stars (inside $\sim 1\,R_e$) in both these groups, and compare for the first time the H I properties of SRs and FRs to predictions from ΛCDM hydrodynamical simulations.

We find a large diversity of H I masses and morphologies within both the FR and SR families. Surprisingly, SRs are detected as often, host as much H I and have a similar rate of H I discs and rings as FRs. The only tentative difference between the two families is that the H I discs/rings around SRs are usually not fully settled. This comparison is mostly limited by the small number of SRs in our sample (simply because these galaxies amount to just ∼15 per cent of the total ETG population) and a larger SR sample would be needed to improve the accuracy of some of the above conclusions. Nevertheless, our data imply that SRs can accrete a significant mass of cold gas during their life, and that they may do so at a rate similar to that of FRs. This is confirmed by the frequent detection of cold dust (Smith et al. 2012), kinematically misaligned ionized-gas (Paper X) and cuspy nuclear light profiles (Paper XXIII) in SRs as well by simulations, which indicate that at least some SRs may have formed during gas-rich mergers (Paper VI, Paper XXV).

The high detection rate of H I discs/rings in galaxies with little or no evidence of an embedded stellar disc – the SRs – indicates that the accretion of H I is not always linked to the growth of an inner stellar disc. Such weak relation between H I and stellar disc is confirmed by the fact that in galaxies with a significant stellar disc component – the FRs – the H I does not always corotate with the stars. On the contrary, we find corotation in just about half of all FRs with an H I disc or ring. The remaining FRs exhibit a variety of kinematical misalignments including cases of polar and counterrotating gas. The family of FRs appears therefore significantly more complex and diverse at large radius than in the inner regions, as concluded also using other kinematical tracers (e.g. Coccato et al. 2009; Pota et al. 2013).

The H I misalignments reveal another possible difference between FRs and SRs: in the latter the H I disc/ring is always polar (or nearly so) relative to the stars. We do not find any SR with a co- or counterrotating H I disc or ring, although we note that such gaseous discs are detected at smaller radius in the ionized-gas phase (Paper X).

In Paper XIII we show that the ETG H I mass and morphology depend to some extent on galaxy stellar mass and environment density. Here we find no additional trends as the H I kinematical misalignment does not seem to be related to the host stellar mass or environment in any obvious way. This complex picture highlights

a diversity of ETG formation histories which may be lost in the relative simplicity of their inner structure.

We find that ΛCDM hydrodynamical simulations (both with and without galactic stellar winds) have difficulties reproducing the H I properties of ETGs. We develop a simple method to define H I in the simulations of Oser et al. (2010) and Hirschmann et al. (2013), and find some clear inconsistencies with the observations. The decline of the H I column density distribution is too shallow, resulting in an average density which is larger than in real ETGs. This causes gas discs with an H I mass comparable to the observations to be too small, while discs whose size is sufficiently large are too massive. Furthermore, none of the simulations is able to produce the many gas-poor ETGs present in the observed sample.

Consistent with the observations, H I discs are found in both simulated FRs and SRs. However, their kinematical misalignment from the stars match the observations only qualitatively. On the one hand, nearly all simulated FRs host corotating H I. The few cases with polar or counterrotating gas exhibit very low levels of stellar rotation (unlike real ETGs). On the other hand, a large fraction of the simulated SRs host corotating H I while none hosts a large, (nearly) polar H I disc as in real SRs. We suggest that a more sophisticated treatment of gas physics and a better understanding of the corresponding feedback processes is needed in the simulations, and we conclude that a better match between observed and simulated galaxies should be achieved before cosmological simulations can be used to understand the origin of the complex H I properties of ETGs.

ACKNOWLEDGEMENTS

PS acknowledges support of a NWO/Veni grant. This work is based on observations obtained with the Westerbork Synthesis Radio Telescope, which is operated by ASTRON (Netherlands Institute for Radio Astronomy) with support from the Netherlands Foundation for Scientific Research (NWO). MC acknowledges support from a Royal Society University Research Fellowship. This work was supported by the rolling grants Astrophysics at Oxford PP/E001114/1 and ST/H002456/1 and visitors grants PPA/V/S/2002/00553, PP/E001564/1 and ST/H504862/1 from the UK Research Councils. RLD acknowledges travel and computer grants from Christ Church, Oxford and support from the Royal Society in the form of a Wolfson Merit Award 502011.K502/jd. RLD is also grateful for support from the Australian Astronomical Observatory Distinguished Visitors programme, the ARC Centre of Excellence for All Sky Astrophysics and the University of Sydney during a sabbatical visit. SK acknowledges support from the Royal Society Joint Projects grant JP0869822. RMMcD is supported by the Gemini Observatory, which is operated by the Association of Universities for Research in Astronomy, Inc., on behalf of the international Gemini partnership of Argentina, Australia, Brazil, Canada, Chile, UK and USA. TN and MBois acknowledge support from the DFG Cluster of Excellence 'Origin and Structure of the Universe'. MS acknowledges support from a STFC Advanced Fellowship ST/F009186/1. (TAD) The research leading to these results has received funding from the European Community's Seventh Framework Programme (/FP7/2007-2013/) under grant agreement no. 229517. MBois has received, during this research, funding from the European Research Council under the Advanced Grant Programme no. 267399-Momentum. LMY acknowledges support from NSF grant AST-1109803. MH acknowledges financial support from the European Research Council under the European Community's Seventh Framework Programme (FP7/2007-2013)/ERC grant agreement no. 202781. The authors acknowledge financial support from ESO.

REFERENCES

Alatalo K. et al., 2013, MNRAS, 432, 1796
Arnold J. A., Romanowsky A. J., Brodie J. P., Chomiuk L., Spitler L. R., Strader J., Benson A. J., Forbes D. A., 2011, ApJ, 736, L26
Arnold J. A. et al., 2013, arXiv:e-prints
Bell E. F., McIntosh D. H., Katz N., Weinberg M. D., 2003, ApJS, 149, 289
Bertola F., Buson L. M., Zeilinger W. W., 1992, ApJ, 401, L79
Bettoni D., Galletta G., García-Burillo S., Rodríguez-Franco A., 2001, A&A, 374, 421
Bieging J. H., Biermann P., 1977, A&A, 60, 361
Bigiel F., Leroy A., Walter F., Brinks E., de Blok W. J. G., Madore B., Thornley M. D., 2008, AJ, 136, 2846
Bois M. et al., 2011, MNRAS, 416, 1654 (Paper VI)
Bregman J. N., Hogg D. E., Roberts M. S., 1992, ApJ, 387, 484
Bureau M., Chung A., 2006, MNRAS, 366, 182
Cappellari M. et al., 2006, MNRAS, 366, 1126
Cappellari M. et al., 2007, MNRAS, 379, 418
Cappellari M. et al., 2011a, MNRAS, 413, 813 (Paper I)
Cappellari M. et al., 2011b, MNRAS, 416, 1680 (Paper VII)
Cappellari M. et al., 2013a, MNRAS, 432, 1709 (Paper XV)
Cappellari M. et al., 2013b, MNRAS, 432, 1862 (Paper XX)
Catinella B. et al., 2010, MNRAS, 403, 683
Chung A., van Gorkom J. H., Kenney J. D. P., Crowl H., Vollmer B., 2009, AJ, 138, 1741
Coccato L. et al., 2009, MNRAS, 394, 1249
Combes F., Young L. M., Bureau M., 2007, MNRAS, 377, 1795
Cortesi A. et al., 2013, A&A, 549, A115
Davies R. L., Efstathiou G., Fall S. M., Illingworth G., Schechter P. L., 1983, ApJ, 266, 41
Davis T. A. et al., 2011, MNRAS, 417, 882 (Paper X)
Davis T. A. et al., 2013, MNRAS, 429, 534
Davis T. A. et al., 2014, MNRAS, submitted
di Serego Alighieri S. et al., 2007, A&A, 474, 851
Duc P.-A. et al., 2011, MNRAS, 417, 863
Emsellem E. et al., 2007, MNRAS, 379, 401
Emsellem E. et al., 2011, MNRAS, 414, 888 (Paper III)
Gallagher J. S., Faber S. M., Balick B., 1975, ApJ, 202, 7
Giovanelli R. et al., 2005, AJ, 130, 2598
Grossi M. et al., 2009, A&A, 498, 407
Hirschmann M., Naab T., Somerville R. S., Burkert A., Oser L., 2012, MNRAS, 419, 3200
Hirschmann M. et al., 2013, MNRAS, 436, 2929
Jorgensen I., Franx M., 1994, ApJ, 433, 553
Józsa G. I. G., Oosterloo T. A., Morganti R., Klein U., Erben T., 2009, A&A, 494, 489
Kartha S. S., Forbes D. A., Spitler L. R., Romanowsky A. J., Arnold J. A., Brodie J. P., 2014, MNRAS, 437, 273
Kawata D., Cen R., Ho L. C., 2007, ApJ, 669, 232
Khochfar S. et al., 2011, MNRAS, 417, 845 (Paper VIII)
Knapp G. R., Gallagher J. S., Faber S. M., Balick B., 1977, AJ, 82, 106
Knapp G. R., Turner E. L., Cunniffe P. E., 1985, AJ, 90, 454
Kormendy J., Bender R., 2012, ApJS, 198, 2
Krajnović D., Cappellari M., de Zeeuw P. T., Copin Y., 2006, MNRAS, 366, 787
Krajnović D. et al., 2011, MNRAS, 414, 2923 (Paper II)
Krajnović D. et al., 2013a, MNRAS, 432, 1768
Krajnović D. et al., 2013b, MNRAS, 433, 2812 (Paper XXIII)
Krumholz M. R., McKee C. F., Tumlinson J., 2009, ApJ, 693, 216
Laurikainen E., Salo H., Buta R., Knapen J. H., 2011, MNRAS, 418, 1452
Lees J. F., Knapp G. R., Rupen M. P., Phillips T. G., 1991, ApJ, 379, 177
Martig M., Bournaud F., Teyssier R., Dekel A., 2009, ApJ, 707, 250
Martig M. et al., 2013, MNRAS, 432, 1914

Morganti R. et al., 2006, MNRAS, 371, 157
Naab T., Johansson P. H., Ostriker J. P., 2009, ApJ, 699, L178
Naab T. et al., 2014, MNRAS, 444, 3357 (Paper XXV)
Oosterloo T. A., Morganti R., Sadler E. M., van der Hulst T., Serra P., 2007, A&A, 465, 787
Oosterloo T. et al., 2010, MNRAS, 409, 500
Oppenheimer B. D., Davé R., 2006, MNRAS, 373, 1265
Oser L., Ostriker J. P., Naab T., Johansson P. H., Burkert A., 2010, ApJ, 725, 2312
Oser L., Naab T., Ostriker J. P., Johansson P. H., 2012, ApJ, 744, 63
Pota V. et al., 2013, MNRAS, 428, 389
Proctor R. N., Forbes D. A., Romanowsky A. J., Brodie J. P., Strader J., Spolaor M., Mendel J. T., Spitler L., 2009, MNRAS, 398, 91
Roberts M. S., 1975, in Sandage A., Sandage M., Kristian J., eds, Radio Observations of Neutral Hydrogen in Galaxies, Univ. Chicago Press, Chicago, p. 309
Romanowsky A. J., Douglas N. G., Arnaboldi M., Kuijken K., Merrifield M. R., Napolitano N. R., Capaccioli M., Freeman K. C., 2003, Science, 301, 1696
Sadler E. M., 2001, in Hibbard J. E., Rupen M., van Gorkom J. H., eds, ASP Conf. Ser. Vol. 240, Gas and Galaxy Evolution. Astron. Soc. Pac., San Francisco, p. 445
Sage L. J., Welch G. A., Young L. M., 2007, ApJ, 657, 232
Saintonge A. et al., 2011, MNRAS, 415, 32
Saintonge A. et al., 2012, ApJ, 758, 73
Schruba A. et al., 2011, AJ, 142, 37
Serra P. et al., 2012, MNRAS, 422, 1835 (Paper XIII)
Sijacki D., Vogelsberger M., Kereš D., Springel V., Hernquist L., 2012, MNRAS, 424, 2999
Smith M. W. L. et al., 2012, ApJ, 748, 123
Springel V., Yoshida N., White S. D. M., 2001, New Astron., 6, 79
van der Hulst J. M., Terlouw J. P., Begeman K. G., Zwitser W., Roelfsema P. R., 1992, in Worrall D. M., Biemesderfer C., Barnes J., eds, ASP Conf. Ser. Vol. 25, Astronomical Data Analysis Software and Systems I. Astron. Soc. Pac., San Francisco, p. 131
van Driel W., van Woerden H., 1991, A&A, 243, 71
van Gorkom J., Schiminovich D., 1997, in Arnaboldi M., Da Costa G. S., Saha P., eds, 2nd Stromlo Symp., ASP Conf Ser. Vol. 116, The Nature of Elliptical Galaxies. Astron. Soc. Pac., San Francisco, p. 310
van Gorkom J. H., Schechter P. L., Kristian J., 1987, ApJ, 314, 457
Wardle M., Knapp G. R., 1986, AJ, 91, 23
Weijmans A.-M. et al., 2009, MNRAS, 398, 561
Weijmans A.-M. et al., 2013, MNRAS, submitted
Welch G. A., Sage L. J., Young L. M., 2010, ApJ, 725, 100
Wiklind T., Henkel C., 1989, A&A, 225, 1
Wong T., Blitz L., 2002, ApJ, 569, 157
Young L. M. et al., 2011, MNRAS, 414, 940 (Paper IV)

APPENDIX A: H I MISALIGNMENT CURVES

Fig. A1 shows the variation of the kinematical misalignment PA(H I) − PA(stars) as a function of radius for the 26 galaxies with extended H I distributions analysed using the KINEMETRY software (Krajnović et al. 2006). This includes all *D*s in the ATLAS^{3D} sample, all *R*s and the two *u* galaxies with some settled gas, NGC 1023 and NGC 4026 (see Section 4). Note that PA(H I) varies as a function of radius while PA(stars) is an average central value, as explained in detail in Section 4. The curves in the figure were used to determine the median misalignment values shown in Fig. 5. Note the severe warps of NGC 2685 and NGC 5173, which are discussed also in Section 4. For these two galaxies the small median misalignment angle is not representative of the true complexity of the gas system. The figure also shows the kinematical misalignment between ionized/molecular gas and stars presented in Paper X. The kinematical alignment between inner H I and other gas phases is discussed in Section 4.1. We refer to the caption of Fig. A1 for more details on its content.

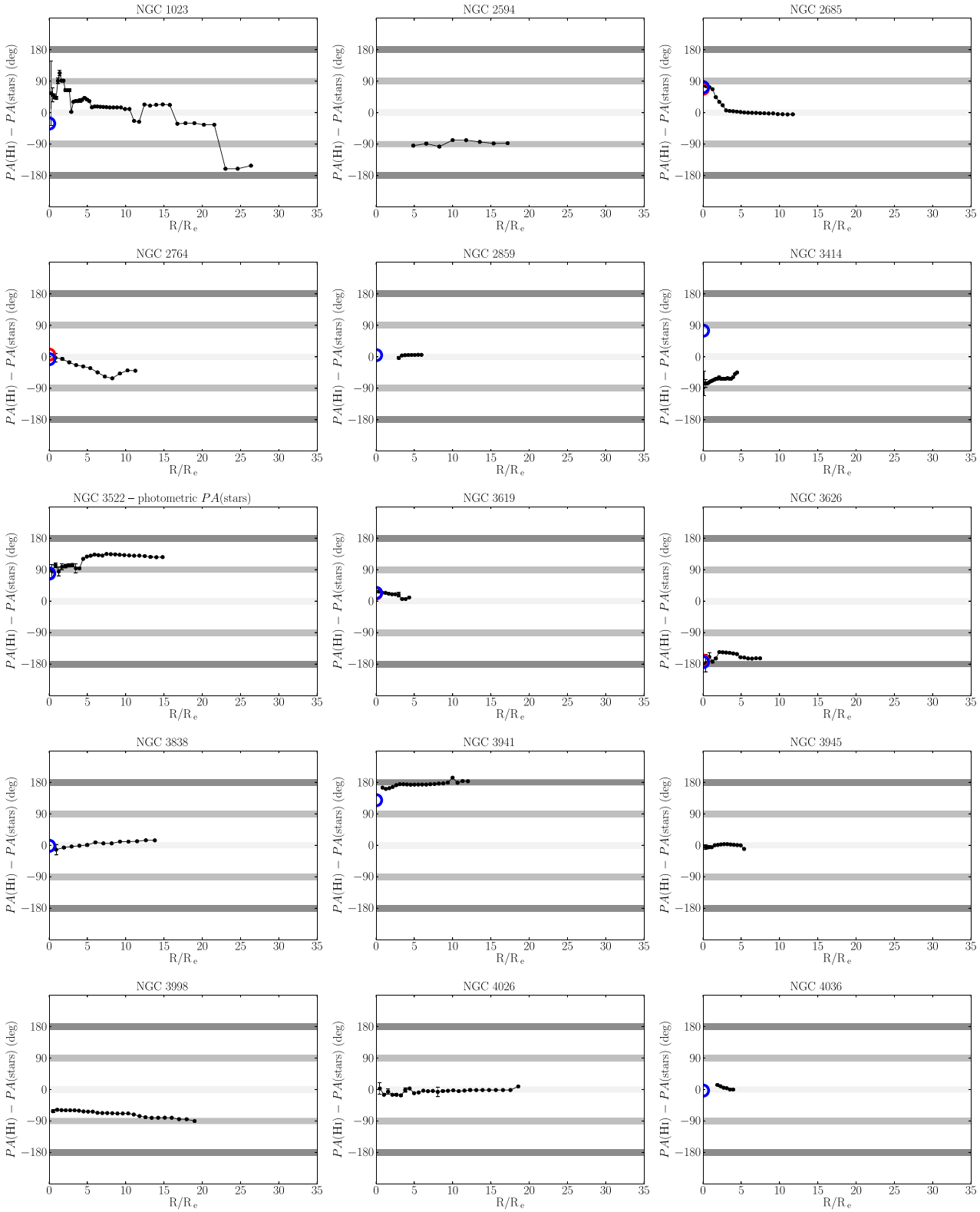

Figure A1. H I misalignment as a function of radius in units of R_e (Paper I). The black dots represent the measurements. The thick, horizontal grey lines serve as a reference to identify gas close to corotation, polar distribution and counterrotation, respectively. We highlight the few cases where PA(stars) is the photometric rather than kinematical PA. Red and blue semicircles at $R = 0$ show molecular and ionized-gas misalignment, respectively.

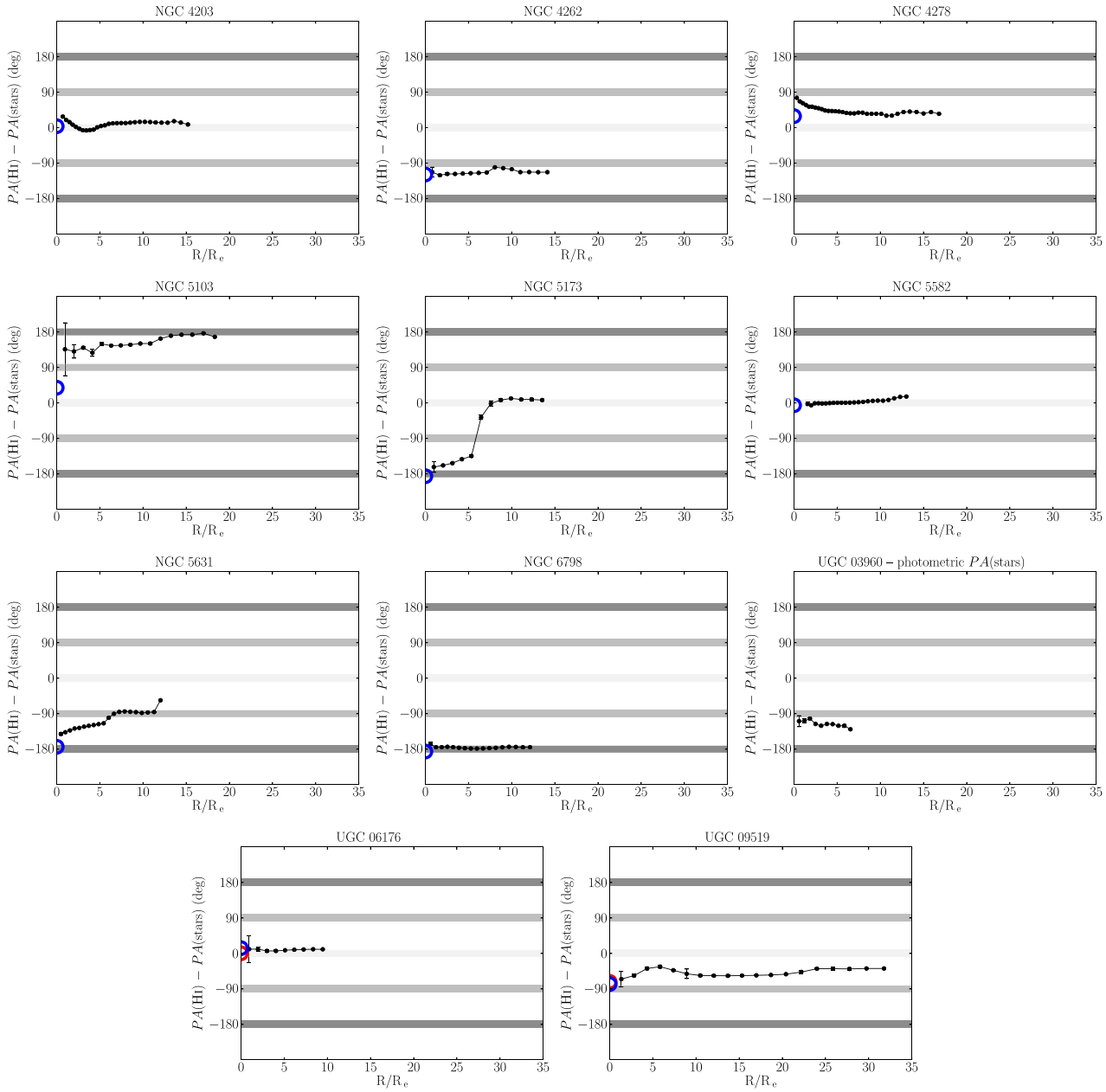

Figure A1 – *continued*

[1]*Netherlands Institute for Radio Astronomy (ASTRON), Postbus 2, NL-7990 AA Dwingeloo, the Netherlands*
[2]*CSIRO Astronomy and Space Science, Australia Telescope National Facility, PO Box 76, Epping, NSW 1710, Australia*
[3]*Max-Planck-Institut für Astrophysik, Karl-Schwarzschild-Str. 1, D-85741 Garching, Germany*
[4]*Department of Astronomy, Columbia University, New York, NY 10027, USA*
[5]*Leibniz-Institut für Astrophysik Potsdam (AIP), An der Sternwarte 16, D-14482 Potsdam, Germany*
[6]*Kapteyn Astronomical Institute, University of Groningen, Postbus 800, NL-9700 AV Groningen, the Netherlands*
[7]*Sub-Department of Astrophysics, Department of Physics, University of Oxford, Denys Wilkinson Building, Keble Road, Oxford OX1 3RH, UK*
[8]*European Southern Observatory, Karl-Schwarzschild-Str. 2, D-85748 Garching, Germany*
[9]*Université Lyon 1, Observatoire de Lyon, Centre de Recherche Astrophysique de Lyon and Ecole Normale Supérieure de Lyon, 9 avenue Charles André, F-69230 Saint-Genis Laval, France*
[10]*Physics Department, New Mexico Institute of Mining and Technology, Socorro, NM 87801, USA*
[11]*Department of Astronomy, Campbell Hall, University of California, Berkeley, CA 94720, USA*
[12]*Laboratoire AIM Paris-Saclay, CEA/IRFU/SAp – CNRS – Université Paris Diderot, F-91191 Gif-sur-Yvette Cedex, France*
[13]*INAF – Astronomical Observatory of Trieste, via G.B. Tiepolo 11, I-34143 Trieste, Italy*
[14]*Dunlap Institute for Astronomy & Astrophysics, University of Toronto, 50 St. George Street, Toronto, ON M5S 3H4, Canada*
[15]*School of Physics and Astronomy, University of St Andrews, North Haugh, St Andrews KY16 9SS, UK*

[16]*Infrared Processing and Analysis Center, California Institute of Technology, Pasadena, CA 91125, USA*
[17]*Ritter Astrophysical Observatory, University of Toledo, Toledo, OH 43606, USA*
[18]*Sterrewacht Leiden, Leiden University, Postbus 9513, NL-2300 RA Leiden, the Netherlands*
[19]*Max-Planck Institut für extraterrestrische Physik, PO Box 1312, D-85478 Garching, Germany*
[20]*Institute for Astronomy, University of Edinburgh, Royal Observatory, Blackford Hill, Edinburgh EH9 3HJ, UK*
[21]*Gemini Observatory, Northern Operations Centre, 670 N. A'ohoku Place, Hilo, HI 96720, USA*
[22]*Centre for Astrophysics Research, University of Hertfordshire, Hatfield, Herts AL1 9AB, UK*
[23]*Sydney Institute for Astronomy (SIfA), School of Physics, The University of Sydney, NSW 2006, Australia*
[24]*ARC Centre of Excellence for All-sky Astrophysics (CAASTRO), 44 Rosehill Street, Redfern, NSW 2016, Australia*

This paper has been typeset from a TEX/LATEX file prepared by the author.